Cancer Letters 635 (2025) 218104

Contents lists available at ScienceDirect

Cancer Letters

journal homepage: www.elsevier.com/locate/canlet

Original Articles

Obese adipose tissue-derived extracellular vesicles enriched with glycolytic cargo promote colorectal cancer tumorigenesis

Parsa S. Haque[a], Sheré L. Paris[b], Rhonda F. Souza[b,c], Joseph C. Onyiah[a,g], Christina Coughlan[d], David J. Orlicky[e], Janos Zempleni[f], Arianne L. Theiss[a,g,*]

[a] Division of Gastroenterology and Hepatology, Department of Medicine, University of Colorado School of Medicine, Aurora, CO, 80045, USA
[b] Center for Esophageal Research, Baylor Scott & White Research Institute, Dallas, TX, 75246, USA
[c] Department of Medicine, Center for Esophageal Diseases, Baylor University Medical Center, Dallas, TX, 75246, USA
[d] Department of Neurology, Department of Medicine, University of Colorado School of Medicine, Aurora, CO, 80045, USA
[e] Division of Pathology, Department of Medicine, University of Colorado School of Medicine, Aurora, CO, 80045, USA
[f] Department of Nutrition and Health Sciences, University of Nebraska-Lincoln, Lincoln, NE, 68583, USA
[g] Rocky Mountain Regional Veterans Affairs Medical Center, Aurora, CO, USA

ARTICLE INFO

Keywords:
EV
Glycolysis
Stem
Tsg101
CRC
Obesity

ABSTRACT

Obesity increases the risk of colorectal cancer (CRC) development, accelerates disease progression and is associated with decreased disease-free survival. Obesity adversely affects the visceral adipose tissue (VAT) leading to increased secretion of extracellular vesicles (EVs). However, the crosstalk between VAT and CRC tumor cells still remains unclear. EVs are lipid-membraned particles that transfer cargo to and/or induce signaling in other cells. Here, we characterized human VAT-derived non-obese (N-OB) and obese (OB) EVs and investigated the functional interaction between CRC cells and VAT-derived EVs. EVs were isolated from VAT obtained from obese (BMI>30) and non-obese patients (BMI<30). Unbiased proteomics revealed that compared to N-OB EVs, OB EVs were enriched with glycolytic enzymes like triose phosphate isomerase (TPI1). This enrichment was associated with increased TPI1 protein levels in CRC cells and elevated glycolytic activity. OB EV-treated cells also exhibited increased stemness-associated genes, 3D-spheroid formation and *Apc*$^{min/+}$ tumoroid self-renewal capacity. *In vivo*, mice with an adipocyte-specific knockout of EV cargo sorting protein, Tsg101 (*Tsg101*$^{\Delta Ad}$), had altered EV cargo composition with reduced glycolytic enzyme levels. Functionally, *Tsg101*$^{\Delta Ad}$-EVs were able to protect against high-fat diet (HFD)-induced increase in glycolysis and stem-like ability. Moreover, *Apc*$^{min/+}$:*Tsg101*$^{\Delta Ad}$ mice were protected against HFD-induced enhanced tumorigenesis. Collectively, this study identifies adipocyte EVs, and their metabolic cargo, as an important regulator of CRC cell metabolism and function, promoting intestinal tumorigenesis.

1. Introduction

Colorectal cancer (CRC) remains the third leading cause of cancer-related deaths in the US, regardless of large-scale screening and advances in treatment options [1]. Confounding factors like obesity complicate both the development and treatment of CRC. CRC prognosis is linked to a patient's body mass index (BMI), with studies indicating that obese patients are more likely to present with advanced-stage CRC [2]. Some studies have reported a reduction in the risk of CRC, up to 54 %, in patients with obesity who have undergone bariatric surgery [3–5]. Furthermore, CRC patients with an obese/overweight BMI are resistant to therapy [6] and exhibit an immunosuppressive tumor microenvironment with a distinct metabolic signature that was more glycolytic compared to normal weight CRC patients [7]. These studies highlight the significant impact of obesity on CRC tumorigenesis and the need for addressing this confounding factor in treatment strategies.

Intestinal stem cells (ISCs) are long-lived cells located at the base of the crypts involved in regulated cycles of division for self-renewal and

---

Abbreviations: Apc, adenomatous polyposis coli; HFD, high-fat diet; ISCs, intestinal stem cells; MD, matched diet; Min, multiple intestinal neoplasia; N-OB, non-obese; OB, obese; Tsg101, tumor susceptibility gene 101; VAT, visceral adipose tissue.

[*] Corresponding author. Division of Gastroenterology and Hepatology, University of Colorado School of Medicine, East 19th Avenue, RC2 Campus Box: B158 HSC, Aurora, Colorado, 12700, USA.

E-mail address: arianne.theiss@cuanschutz.edu (A.L. Theiss).

https://doi.org/10.1016/j.canlet.2025.218104
Received 1 April 2025; Received in revised form 2 October 2025; Accepted 27 October 2025

generate committed daughter progenitor cells that undergo differentiation to maintain intestinal epithelial structure and integrity [8]. ISCs are maintained by a high WNT signaling gradient at the base of the crypt [9]. According to the 'bottom-up' model of CRC, DNA mutations in key driver genes in long-lived ISCs are essential in neoplastic transformation of colonic cells, with mutations in *APC* occurring as an early or as an initial step in tumor progression for ~80 % of sporadic microsatellite stable (MSS) CRCs [9,10]. Several studies in mice have shown that high-fat diet (HFD) feeding promoted gut microbial dysbiosis, increased gut permeability, ISC hyperproliferation, self-renewal capacity and enhanced tumorigenic potential [11–14]. Importantly, HFD directly changed ISC function via activation of peroxisome proliferator-activated receptor (PPAR)-dependent fatty acid oxidation (FAO) and led to their enhanced capacity to initiate intestinal tumors in mice during *Apc*-deficiency [12,13]. HFD was also shown to promote ISC proliferation via increased levels of bile acids which, in turn, inhibited farnesoid X receptor (FXR) signaling in ISCs to promote CRC progression [11]. Additionally, HFD enhanced glycolysis in mesenchymal stromal cells, supporting WNT signaling to ISCs, thereby driving stemness in mouse colonic crypts [15]. These studies suggest that HFD affects stem-like characteristics and metabolism of colonic cells to enhance CRC initiation and progression.

In addition to these intestinal effects of HFD, HFD feeding as a model of obesity leads to deposition of excess visceral adipose tissue (VAT) in the abdominal organs, including small intestine and colon, which can also influence tumorigenesis and promote resistance to conventional anti-cancer therapies [6,16]. Research in a xenograft mouse model of CRC demonstrated that HFD-induced obesity activated pro-oncogenic signaling pathways resulting in tumor growth and progression [17], suggesting systemic signaling to the tumor cells beyond direct effects of the diet in the intestine. In this regard, previous studies pertaining to the role of obese VAT in CRC development or progression have focused on secreted lipids or adipokines in driving disease [18–20].

Extracellular vesicles (EVs) are 50–1000 nm sized lipid-membraned particles that are emerging as important signaling mediators of local and distant cellular communication. EVs contain nucleic acids, proteins and lipids as cargo and have been found to transport their contents to or induce various signaling pathways in target cells [21]. Obesity phenotypically changes VAT, increases EV secretion and is associated with altering the composition of EV cargo [22,23]. In fact, we and others have shown that EVs released from obese VAT are enriched in metabolic enzymes [24], oncogenic proteins or miRNA that are actively taken up by cancer cells for their survival [21]. Recent studies have primarily focused on the role of AT derived-EVs on breast [25,26], melanoma [18,27] and ovarian cancer [28], owing to their vicinity to AT depots. Metabolically active obese AT was shown to transport its energy reserves of lipids, metabolic enzymes and miRNAs to cancer cells via EVs, effectively reprogramming tumor energy metabolism to support growth [21]. Since metabolism regulates cancer stem-like cell survival [13], EVs can also play a role in supporting the expansion of the cancer stem-like cell population. Therefore, we propose that VAT-derived obese EVs regulate CRC cell metabolism and stem-like ability to create an environment conducive to tumor development.

In the current study, we characterized human VAT-derived non-obese (N-OB) and obese (OB) EV cargo and its interactions with CRC cells. We reveal that VAT-derived OB EVs are enriched with glycolytic enzymes, in particular Triose Phosphate Isomerase 1 (TPI1) which catalyzes the interconversion of dihydroxyacetone phosphate and glyceraldehyde-3-phosphate in glycolysis, a key step in driving the glycolytic pathway [29]. OB EVs with altered metabolic cargo reprogram CRC metabolism towards glycolysis and promote stem-like ability. During EV biogenesis, the endosomal sorting complex required for transport (ESCRT) machinery recruits tumor susceptibility gene 101 (Tsg101) as a scaffold protein to enable EV formation from late endosomes. More importantly, Tsg101 has a ubiquitin-recognition domain which binds to and recruits ubiquitinated cargo to the endosomal membrane, leading to protein cargo incorporation into EVs [30]. Therefore, to alter EV protein cargo, we knocked down Tsg101 in mouse adipocytes, resulting in secretion of adipocyte-EVs ($Tsg101^{\Delta Ad}$- EVs) lacking glycolytic enzymes. CRC cells exposed to $Tsg101^{\Delta Ad}$- EVs are protected from HFD-driven glycolysis and stem-like ability *in vitro*. Moreover, $Apc^{min/+}$:$Tsg101^{\Delta Ad}$ mice were protected from HFD-driven polyp formation and enhanced crypt proliferation, underscoring the detrimental role of obese adipocyte-derived EVs in early stages of CRC development.

2. Results

2.1. Obesity increases the secretion of OB EVs packaged with glycolytic enzymes

Obese VAT is associated with greater health risks compared to other AT depots owing to its high metabolic activity and location around major abdominal organs [31]. Moreover, VAT secretes higher number of EVs enriched with more protein cargo than other depots such as subcutaneous adipose tissue [22]. Therefore, we obtained human VAT surrounding the abdominal organs from non-obese (BMI<30) patients and patients with obesity (BMI>30) (Table 1). Isolated VAT was *ex vivo* cultured for collection of conditioned media. VAT conditioned media was processed through ultracentrifugation to isolate N-OB and OB EVs (Fig. 1A). The size and concentration of ultracentrifugation-isolated human VAT samples were quantified through nanoparticle tracking analysis (NTA) and based on their size distribution (50–350 nm) (Fig. 1B), our VAT samples were a heterogenous mixture of small and intermediate-sized vesicles which we will call EVs herein. [32]. NTA results also revealed that human obese VAT released significantly higher number of EVs than non-obese VAT (Fig. 1B), as has been reported previously [22]. We also visualized EV morphology and size through transmission electron microscopy (Fig. 1C) which showed the classical "cup-shaped" morphology typical of adipocyte-derived EVs [33,34]. EVs, irrespective of BMI, express common EV markers like Tsg101 and CD9 along with adipocyte-specific marker, adiponectin, confirming their cell-of-origin (Fig. 1D). Furthermore, confocal microscopy of EV-treated HCT-116 cells showed that both N-OB and OB EVs enter CRC cells within 24 h of treatment (Fig. 1E–S1A).

To interrogate the protein cargo packaged within VAT-derived EVs, we performed unbiased proteomics on human N-OB and OB EVs. We identified a total of 300 human EV proteins (Table S1), of which OB EV had 144 unique proteins (Fig. 2A, Table S2). Panther analysis revealed that 37 % of human VAT-derived EV proteins were associated with metabolism (Fig. 2B), similar to plasma exosome cargo isolated from obese and normal-weight CRC patients [35]. Specifically, proteins associated with the metabolic pathway glycolysis were significantly upregulated in human OB EV compared to N-OB EV (Fig. 2C–Table S3). As an additional model of obesity, we administered a purified high-fat diet (HFD) to C57BL/6 J mice fed over a 16-week period compared to mice fed a matched control diet low in fat [24]. Similar to human OB EVs, EVs isolated from VAT of mice fed HFD (OB EV) exhibited

Table 1
Demographics of patients.

	Body-mass index (BMI)	Age	Sex	Race	
Patient 1	24.5	48	M	Caucasian	Non-Obese
Patient 2	26.6	53	M	Caucasian	
Patient 2	27.3	57	F	Hispanic	
Patient 3	28.3	63	F	Caucasian	
Patient 4	45	26	M	African American	Obese
Patient 5	46	33	F	Caucasian	
Patient 6	48	54	M	Caucasian	
Patient7	74	59	M	Caucasian	

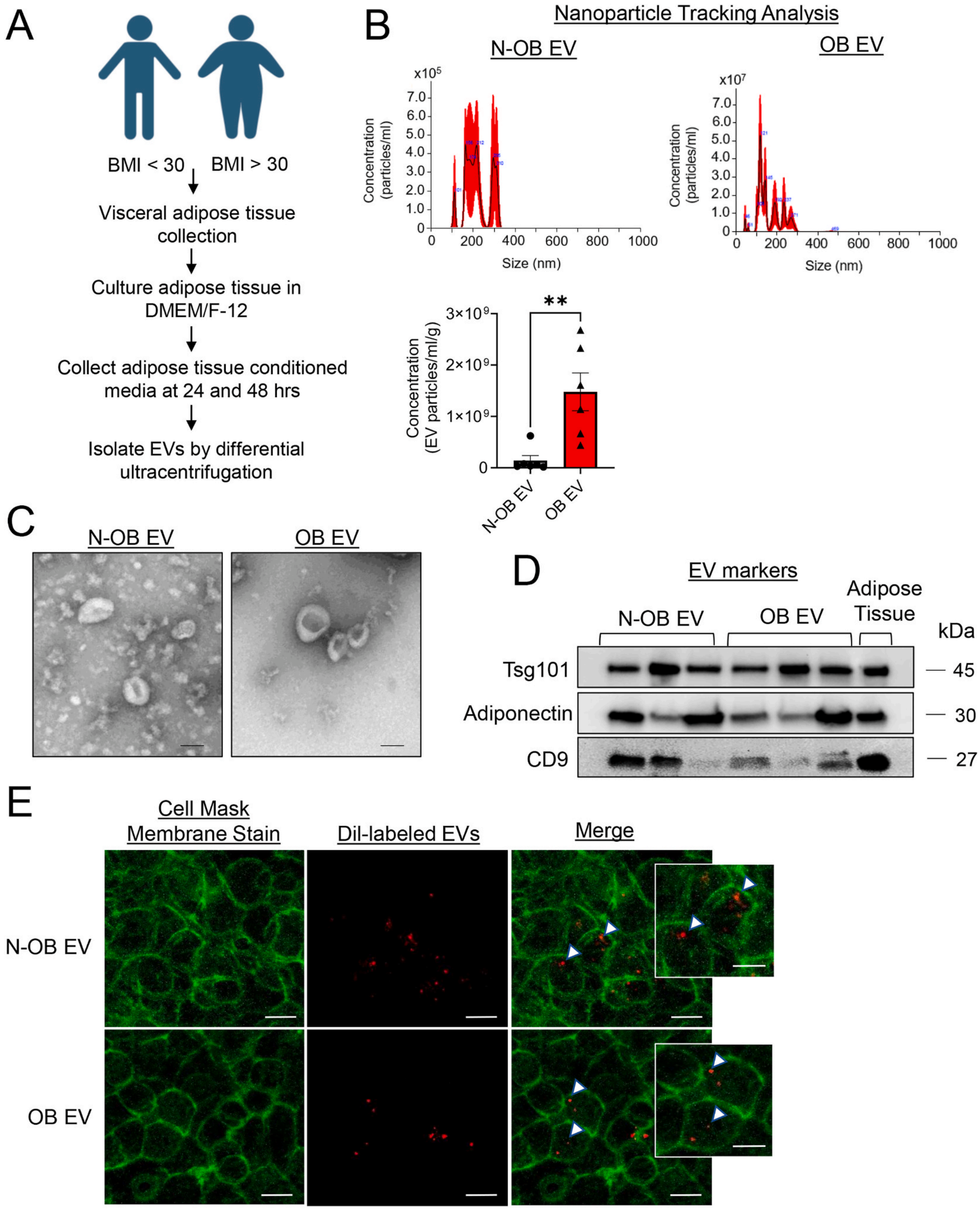

Fig. 1. Characterization of human visceral adipose tissue derived OB EVs. (A) Workflow of EV isolation from VAT of human obese (BMI>30) and non-obese (BMI<30) patients. (B) Representative nanoparticle tracking analysis (top) and concentration of human N-OB and OB EVs normalized to VAT weight (bottom); biological replicate for EV concentration bar graph, n = 6/group (right). (C) Representative transmission electron microscopy images (TEM) of isolated EVs. Bar = 100 nm. (D) Western blots of established EV markers in human OB and N-OB EVs, biological replicate, n = 3/group. (E) Representative confocal microscopy z-stack images after HCT-116 were incubated with of Dil-labeled (red) EVs (arrowheads) for 24 h. Cell membrane was stained with Cell Mask Plasma Membrane Stain (Green). Bar = 10 μm; inset bar = 15 μm. (For interpretation of the references to color in this figure legend, the reader is referred to the Web version of this article.)

upregulation of proteins associated with glycolysis (Fig. 2C–Table S4). Further dissection of this pathway revealed that OB EVs, irrespective of species, were enriched with different glycolytic enzymes (Fig. 2D). These results indicate that obesity increases glycolytic proteins in VAT-derived OB EVs.

2.2. OB EVs increase glycolysis and stem-like properties of CRC cells

Considering the metabolic cargo of the isolated OB EVs, we evaluated whether these EVs resulted in metabolic change in CRC cells. Accordingly, we determined the lowest dose of EVs that elicited maximal metabolic response in human HCT-116 (10^7 EV particles/ml) (Fig. S1B) and mouse MC-38 CRC cells (10^8 EV particles/ml) (Fig. S1C) and performed subsequent experiments using the selected doses appropriate for each species. To interrogate the metabolic profile of CRC cells, we conducted an ATP rate assay and found that EVs, irrespective of BMI, increased ATP production rate (Fig. 3A, S1D) and pushed CRC metabolism towards a glycolytic phenotype in different CRC cell lines (Fig. 3B–S1E-G). By conducting a glycolytic rate assay, which measures both basal and compensatory glycolysis, we confirmed that human OB EVs, but not N-OB EVs, increased the glycolytic capacity of CRC cells (Fig. 3C–S1H, I). Of note, OB EVs upregulated glycolysis to levels similar

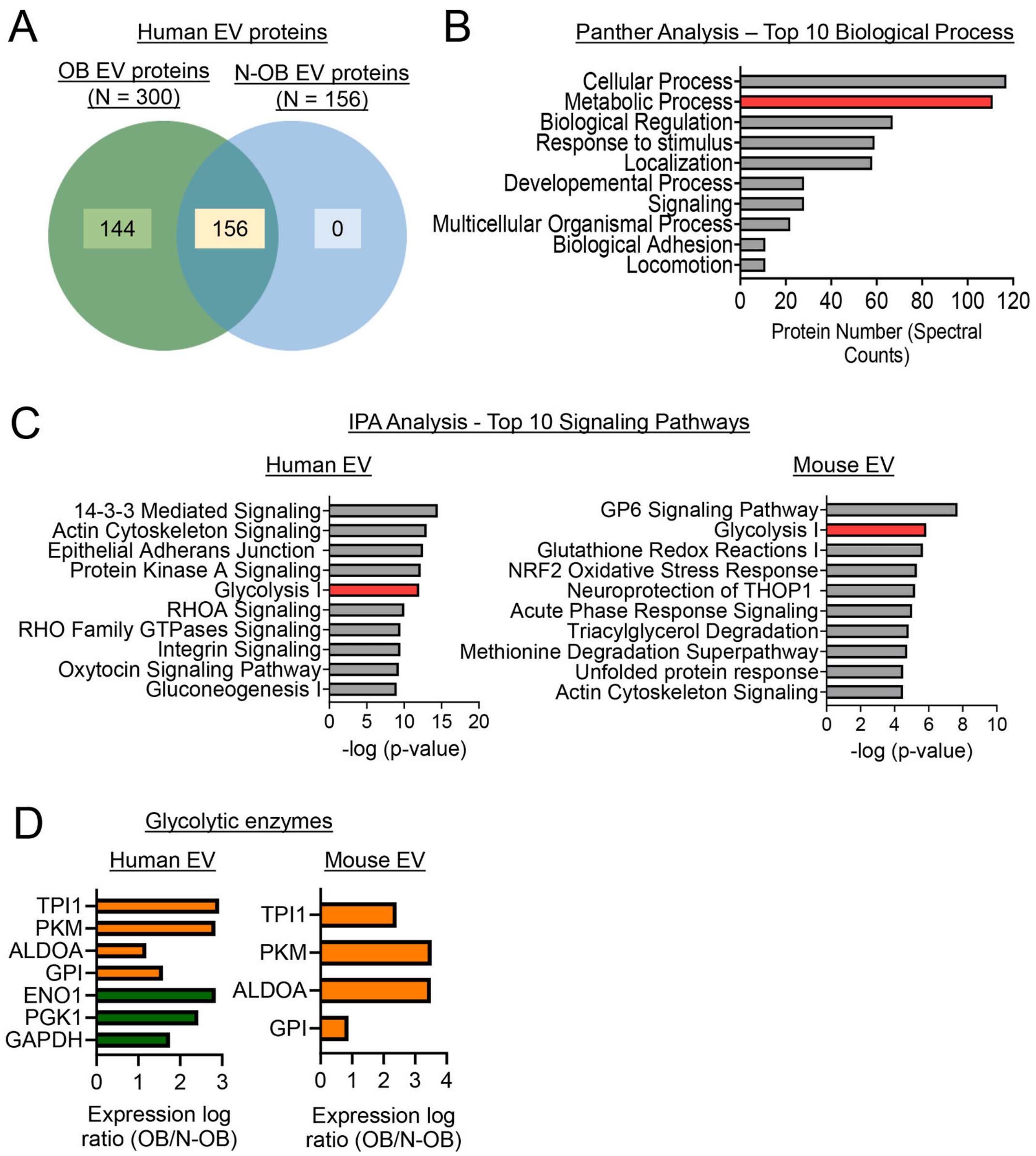

Fig. 2. Proteomic characterization reveals an enrichment of glycolytic enzymes in OB EVs. (A) Venn Diagram of overlapping proteins between OB- (green) and N-OB EVs (blue); biological replicate, n = 3/group. Venn diagram generated by Jvenn. (B) Panther classification based on biological processes for all EV proteins detected by unbiased proteomics. (C) Ingenuity pathway analysis (IPA) classification of top upregulated signaling pathways in human (left) and mouse (right) OB EVs compared to N-OB EVs. (D) Enrichment of glycolytic enzymes in human (left) and mouse (right) OB EVs identified by IPA analysis. Orange bars represent common enzymes between two species. (For interpretation of the references to color in this figure legend, the reader is referred to the Web version of this article.)

to insulin, a known positive regulator of cellular glycolysis (Fig. S1I) [36], suggesting that OB EVs induce glycolysis to maximal capacity of CRC cells as have been previously described for insulin [37]. Mouse MC-38 cells treated with mouse N-OB or OB EVs also exhibited increased glycolysis, with the highest basal glycolysis induction elicited by OB EVs (Fig. 3D). This is significant since CRC cells utilize glucose for growth, survival and progression [38] and our data indicates that obesity exacerbates this glycolytic phenotype through intercommunication with OB EVs.

Next, we investigated whether the OB EV-induced increase in glycolysis was due to an elevation of glycolytic enzymes in CRC cells since our proteomic analysis demonstrated that EVs packaged glycolytic enzymes. Using the glycolytic enzyme Triosephosphate isomerase (TPI1) as a representative marker for the glycolytic cargo within EVs, we conducted Western blot on human and mouse EV-treated cells. OB EVs, but not N-OB EVs, increased TPI1 protein levels in CRC cells (Fig. 3E and F). An increase in enzyme protein level in treated cells could manifest by induction of endogenous transcription or transfer of exogenous mRNA or protein cargo from OB EVs. Analysis of RNA-seq data indicated that OB EVs do not transcriptionally increase TPI1 in HCT-116 cells (Fig. 3G), suggesting that OB EVs do not transfer TPI1 mRNA as cargo or induce endogenous transcriptional activation of TPI1 but could transfer TPI1 protein exogenously. EVs isolated through ultracentrifugation are limited by potential contamination of non-vesicular entities. To confirm that the induction of TPI1 protein was from bona fide EV cargo and not from non-vesicular entities, we subjected our human and mice ultracentrifugation-isolated EVs through qEV size exclusion chromatography (SEC) – column and validated EV marker and TPI1 expression in pooled SEC fractions (Fig. S2A). qEV SEC-columns can separate non-vesicular entities and reduce lipoproteins from EV samples to increase purity [39,40]. Accordingly, HCT-116 cells treated with SEC-isolated EVs demonstrated an increase in TPI1 specific to OB EVs (Fig. S2B),

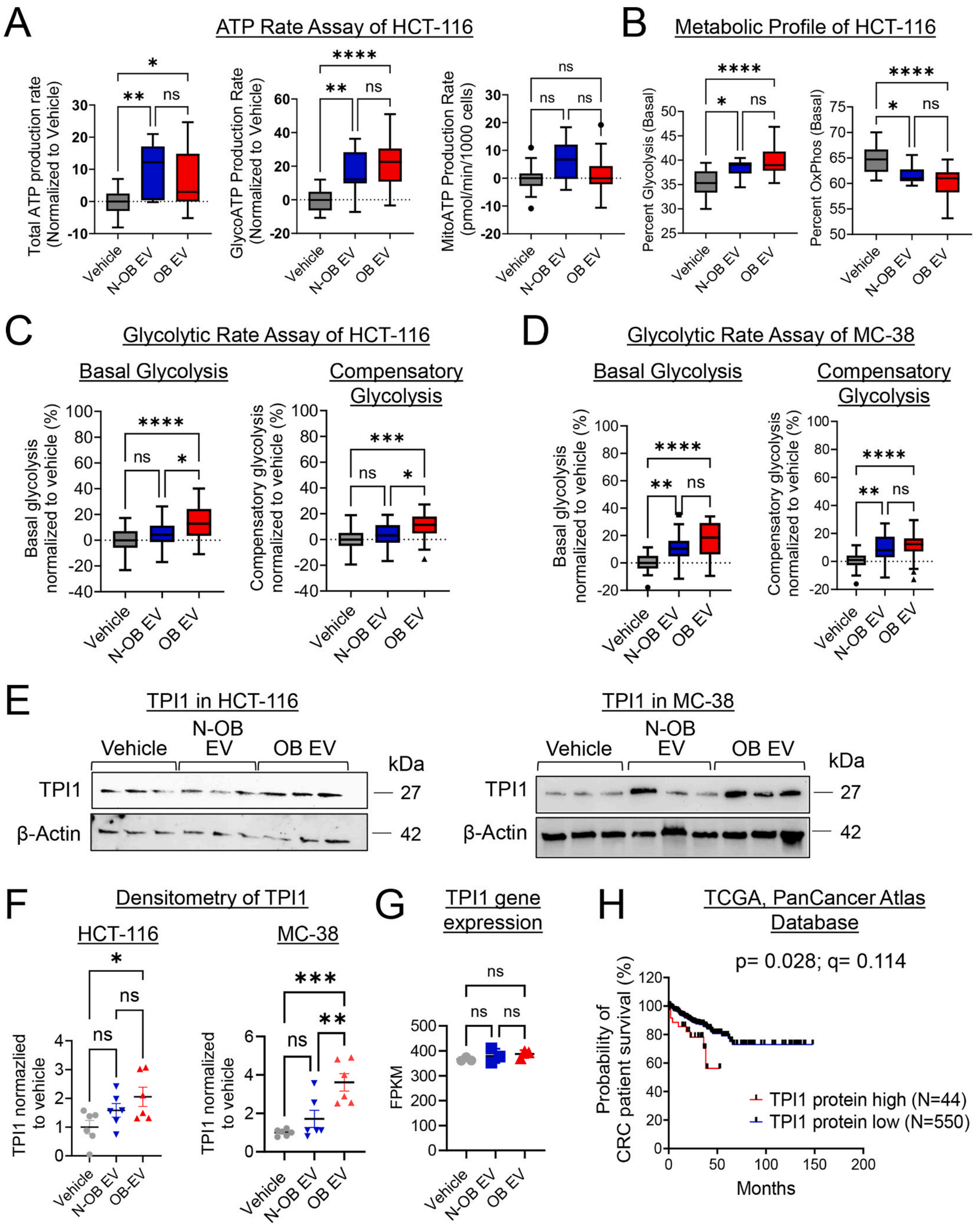

Fig. 3. OB EVs dysregulate metabolism by increasing glycolytic rate of CRC cells. (A) Seahorse XF real-time ATP rate analysis of HCT-116 cells. Total (left), glycolytic (middle) and mitochondrial (right) ATP production rate of HCT-116 after treatment with vehicle, N-OB or OB EVs for 24 h. (B) Metabolic profile of HCT-116 generated by ATP rate analysis. ATP rate assay data is presented as mean of two independent experiments. (C) Seahorse XF real-time Glycolytic rate analysis of HCT-116 cells. Basal (left) and compensatory (right) glycolysis of HCT-116 after treatment with vehicle, N-OB or OB EVs for 24 h. Data is presented as mean of three independent experiments. (D) Seahorse XF real-time Glycolytic rate analysis of MC-38 cells. Basal (left) and compensatory (right) glycolysis of MC-38 cells after treatment with vehicle, N-OB or OB EVs for 24 h. Data is presented as mean of three independent experiments. (E) Western blot images of TPI1 after 24 h treatment of HCT-116 (left) or MC-38 (right) cells with vehicle, N-OB or OB EV. Images are representative of two independent experiments with technical replicates of n = 3 per group/experiment. (F) Densitometric quantification of TPI1 of HCT-116 (left) or MC-38 (right). (G) HCT-116 cells were treated with vehicle, N-OB or OB EVs for 48 h for RNA-seq analysis. TPI1 Fragments Per Kilobase of transcript per Million mapped (FPKM) reads were obtained from RNA-seq analysis. (H) Kaplan-Meier survival plot of TPI1 protein high (N = 44) and low (N = 550) patients based on TCGA's PanCancer Atlas database, p = 0.028 and q = 0.114. All data were analyzed by one-way ANOVA with Tukey's posthoc analysis $*p < 0.05$, $** \leq 0.01$, $*** \leq 0.001$, $**** \leq 0.0001$, ns = not significant.

suggesting that the observed increase in protein levels was not due to non-vesicular TPI1 transfer to CRC cells. In the context of CRC, these results are important since CRC patients with high TPI1 protein expression have a lower probability of survival (Fig. 3H). Taken together, our data suggests that OB EVs drive CRC metabolism toward glycolysis, and that this is associated with an upregulation of glycolytic enzyme protein levels in CRC cells.

To study the transcriptomic changes elicited by EVs, we conducted RNA-seq on HCT-116 cells treated with human N-OB and OB EVs. In agreement with our previous data (Fig. 3A–D), we observed an upregulation of glycolytic genes along with a simultaneous downregulation of genes associated with the electron transport chain in OB EV treated

HCT-116 compared to vehicle (Fig. S2C and D). Importantly, compared to N-OB EV, OB EV increased genes associated with the prominent CRC stemness pathway, Notch signaling pathway (Fig. 4A). Heatmap of Notch signaling genes further showed how this increase is specific to OB EV treatment (Fig. 4B). To functionally validate this signaling phenotype, we conducted a spheroid formation assay since this assay inhibits monolayer formation and only cells with stem-like properties can survive in suspension. In line with the RNA-seq data, OB EVs increased spheroid number compared to N-OB EV (Fig. 4C). We also conducted an *in vitro* limiting dilution assay by seeding HCT-116 cells at low densities and demonstrated that OB EVs increase spheroid number (Fig. 4D) and stem cell frequency (Tables 2–5) even at reduced cell numbers. Specifically, spheroids treated with OB EVs had 2.7 times increase in stem cell frequency compared to N-OB EV (Table 5). Next, we validated our

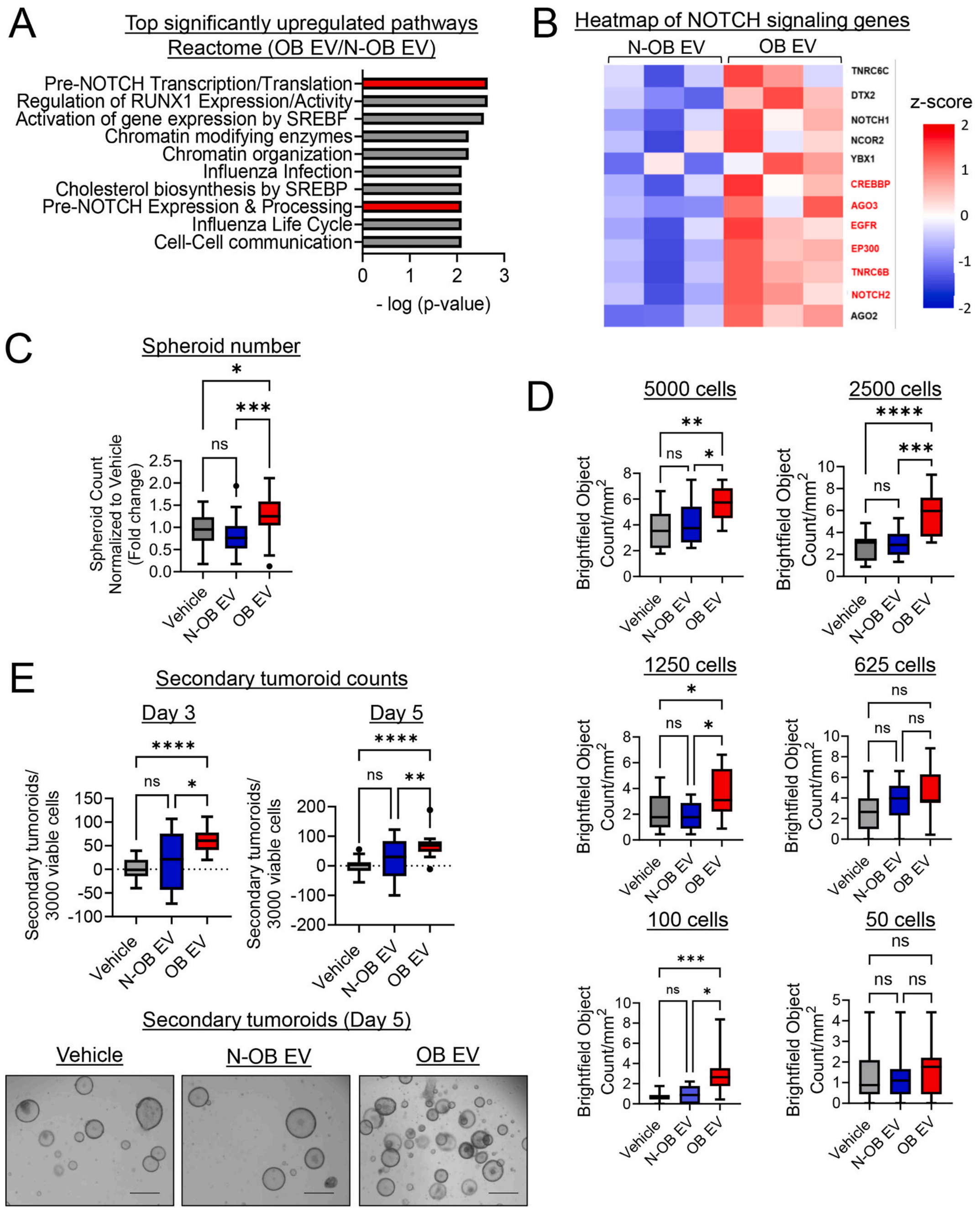

Fig. 4. OB EVs increase stem-like properties of CRC cells. (A) HCT-116 cells were treated with vehicle, N-OB or OB EVs for 48 h for RNA-seq analysis. Bar graph depicts top significantly upregulated pathways in Ob EV-treated HCT-116 based on Reactome pathway database. Technical replicate, n = 3/group. (B) Heatmap shows abundance of NOTCH associated genes in OB EV-treated cells. Red colored genes highlight significantly upregulated genes. (C) HCT-116 spheroids were treated with vehicle, N-OB or OB EVs on alternate days and imaged by Incucyte on day 3. Data is presented as mean of three independent experiments and two biological replicates. (D) HCT-116 spheroids were cultured at progressively low cell doses to conduct *in vitro* limited dilution assay and treated as (A). (E) $Apc^{min/+}$ primary tumoroids were treated with vehicle, N-OB or OB EV on alternate days and secondary tumoroids were established on day 4. Secondary tumoroids were quantitated on day 3 and 5 (top) and representative images (bottom) of secondary tumoroids at 10X, bar = 300 μm. Data is presented as mean of three independent experiments. Data was analyzed using Kruskal-Wallis test with Dunn's post-hoc (C and E) and by one-way ANOVA with Tukey's post-hoc analysis (D). $^{*}p < 0.05$, $^{**}\leq 0.01$, $^{***}\leq 0.001$, $^{****}\leq 0.0001$, ns = not significant. (For interpretation of the references to color in this figure legend, the reader is referred to the Web version of this article.)

Table 2
Positive spheroid formation at limitting cell doses after Vehicle, N-OB and OB EV treatment.

Treatment	Cell dose	Positive response (total number of wells)
Vehicle	5000	16 (16)
	2500	14 (16)
	1250	12 (16)
	625	12 (16)
	100	2 (16)
	50	6 (16)
N-OB EV	5000	12 (12)
	2500	12 (12)
	1250	8 (12)
	625	10 (12)
	100	5 (12)
	50	6 (12)
OB EV	5000	12 (12)
	2500	12 (12)
	1250	11 (12)
	625	11 (12)
	100	10 (12)
	50	7 (12)

Table 3
Overall test for differences in stem cell frequencies between any group.

Chisq	DF	P-value
25.5	2	2.89E-06

Table 4
Pairwise tests for differences in stem cell frequencies.

Treatment 1	Treatment 2	Pr(>Chisq)
Vehicle	N-OB EV	0.0912
Vehicle	OB EV	4.40E-07
N-OB EV	OB EV	0.000871

Table 5
Confidence intervals for 1/stem cell frequency.

Treatment	Lower	Estimate	Upper
Vehicle	998	693	480.8
N-OB EV	696	443	282.2
OB-EV	283	164	94.4

results in a biologically relevant model and established tumoroids from the spontaneous CRC *Apc*$^{min/+}$ model. Primary tumoroids treated with OB EVs gave rise to significantly higher numbers of secondary tumoroids compared to N-OB EVs as early as day 3 (Fig. 4E), suggesting increased self-renewal capacity due to exposure to OB EVs. OB EV-treated primary tumoroids also exhibited increased levels of *Egfr* (Fig. S2E), in accordance with our RNA-seq analysis (Fig. 4B) and frequently upregulated in CRC stem-like cells [41]. These results demonstrate that OB EVs increase stem-like ability of cancer cells in multiple *in vitro* models of CRC.

2.3. *Mice with deletion of adipocyte-specific Tsg101 secrete EVs with altered proteome cargo, counteracting HFD-driven pro-oncogenic effects*

Previously, we observed that HFD-induced obesity was associated with increased expression of the ESCRT1 complex protein Tsg101 in VAT [24]. We generated a novel mouse deficient in adipocyte-specific *Tsg101* expression (*Tsg101*$^{\Delta Ad}$ mice) to alter EV cargo composition (Fig. 5A). This mouse model was fully validated in our previous publication [24] and we observed that while *Tsg101* deletion does not alter the size and morphology of adipocyte EVs (Fig. S3A–B), it results in a deficiency of multiple proteins in *Tsg101*$^{\Delta Ad}$-EVs compared to *Tsg101*$^{fl/fl}$-EVs (Fig. S3C, Table S5) [24]. In fact, 58 % (MD) [24] or 36 % (HFD) of the total proteins were downregulated in *Tsg101*$^{\Delta Ad}$-EVs compared to *Tsg101*$^{fl/fl}$-EVs while only 15 % of proteins (both diets) were upregulated in *Tsg101*$^{\Delta Ad}$-EVs (Table S6) [24]. The deficiency of EV proteins in *Tsg101*$^{\Delta Ad}$ mice resulted in significant downregulation of multiple IPA defined-diseases or functions associated with pro-oncogenicity, like migration of cells or cell viability of tumor cells, irrespective of diet (Fig. 5B–Tables S7–8). Interestingly, among the downregulated proteins, we observed a decrease in several glycolytic enzymes including TPI1, in EVs secreted from *Tsg101*$^{\Delta Ad}$ mice, irrespective of diet (Fig. 5C). These data suggest that *Tsg101* knockdown in the adipocytes alter the proteome within *Tsg101*$^{\Delta Ad}$-EVs, rendering them with a cargo deficient of glycolytic enzymes compared to *Tsg101*$^{fl/fl}$-EVs.

Considering our previous data demonstrating that OB EVs from WT mice increased glycolysis (Fig. 3D) and stem-like ability of CRC cells (Fig. 4C–E), we next tested whether HFD-fed *Tsg101*$^{\Delta Ad}$ mice VAT EVs, with altered EV cargo and reduced levels of glycolytic enzymes, exhibited dampened pro-oncogenic effects (enhanced glycolysis and stem-cell renewal capacity) compared to *Tsg101* $^{fl/fl}$ VAT EVs. Similar to HFD-fed WT OB EVs (Fig. 3D; Fig. 4E), HFD-fed *Tsg101*$^{fl/fl}$-EVs increased basal and compensatory glycolysis in MC-38 cells (Fig. 5D) and secondary tumoroid formation as early as day 3 (Fig. 5E–S2D). Conversely, HFD-fed *Tsg101*$^{\Delta Ad}$-EVs failed to increase glycolytic or stem-like ability of CRC cells (Fig. 5D, E, S3D). These results suggest that *Tsg101*-deficient adipocytes release EVs with decreased glycolytic enzymes as cargo that exhibit dampened ability to induce HFD-driven glycolysis and stem-like properties in CRC cells.

To assess the role of EVs in an *in vivo* CRC model, we crossed our *Tsg101*$^{\Delta Ad}$ mice with *Apc*$^{min/+}$ mice to generate a spontaneous mouse model of CRC secreting adipocyte-EVs with an altered proteomic cargo (*Apc*$^{min/+}$*:Tsg101*$^{\Delta Ad}$) (Fig. 5F). Previous reports demonstrated that HFD increases stem-like potential of colonic cells in *Apc*$^{min/+}$ mice and elevated their ability to form primary colonoids [12]. To investigate whether *Apc*$^{min/+}$*:Tsg101*$^{\Delta Ad}$ mice, with altered adipocyte-EV cargo, can counteract HFD-driven stemness, we fed *Apc*$^{min/+}$*:Tsg101*^{flfl} and *Apc*$^{min/+}$*:Tsg101*$^{\Delta Ad}$ mice HFD and conducted primary colonoid formation and stem cell renewal assay. As expected, we observed a decrease in primary colonoid formation per crypt (Fig. 5G) and secondary colonoid (Fig. 5H–S3E) formation in HFD-fed *Apc*$^{min/+}$*:Tsg101*$^{\Delta Ad}$ mice. Thus, our results indicate that adipocyte EVs play an important role in regulating intestinal stemness in *Apc*$^{min/+}$ crypts.

2.4. *Adipocyte EVs promote colonic polyp formation during HFD*

The *Apc*$^{min/+}$ mice is a mouse model of intestinal tumorigenesis which recapitulates the early stages of sporadic CRC through adenomatous polyp formation, which is also observed in patients. [42–44], When challenged with HFD, intestinal polyps in *Apc*$^{min/+}$ mice progress to adenocarcinoma [14,45]. Since our *in vitro* results indicated that EVs regulate stem-like ability that has been linked to tumor initiation [12], the *Apc*$^{min/+}$ mice serve as an ideal model to study EV-mediated effects in early stages of tumorigenesis during obesity. Measurement of total polyp counts (combination of small and large intestinal polyps) and polyp diameter revealed that HFD-fed *Apc*$^{min/+}$*:Tsg101*^{flfl} mice have a significantly higher number of polys that reach a larger size compared to MD-fed mice (Fig. 6A), as observed in previous studies showing exacerbation of tumorigenesis by HFD [14,45]. However, these effects were attenuated in *Apc*$^{min/+}$*:Tsg101*$^{\Delta Ad}$ mice when challenged with HFD, but not during MD feeding (Fig. 6A), indicating that the role of VAT-derived EVs is significant during the context of obesity or HFD feeding. Upon quantitation of polyp counts based on anatomical location, we observed that *Tsg101* knockdown significantly reduced colonic polyps during HFD but not small intestinal polyps, suggesting a site-specific biological effect in the colon (Fig. 6B). Furthermore, a higher percent of HFD-fed *Apc*$^{min/+}$*:Tsg101*^{flfl} mice developed colonic polyps that progressed to intramucosal adenocarcinoma compared to *Apc*$^{min/+}$*:Tsg101*$^{\Delta Ad}$ (22.2 vs

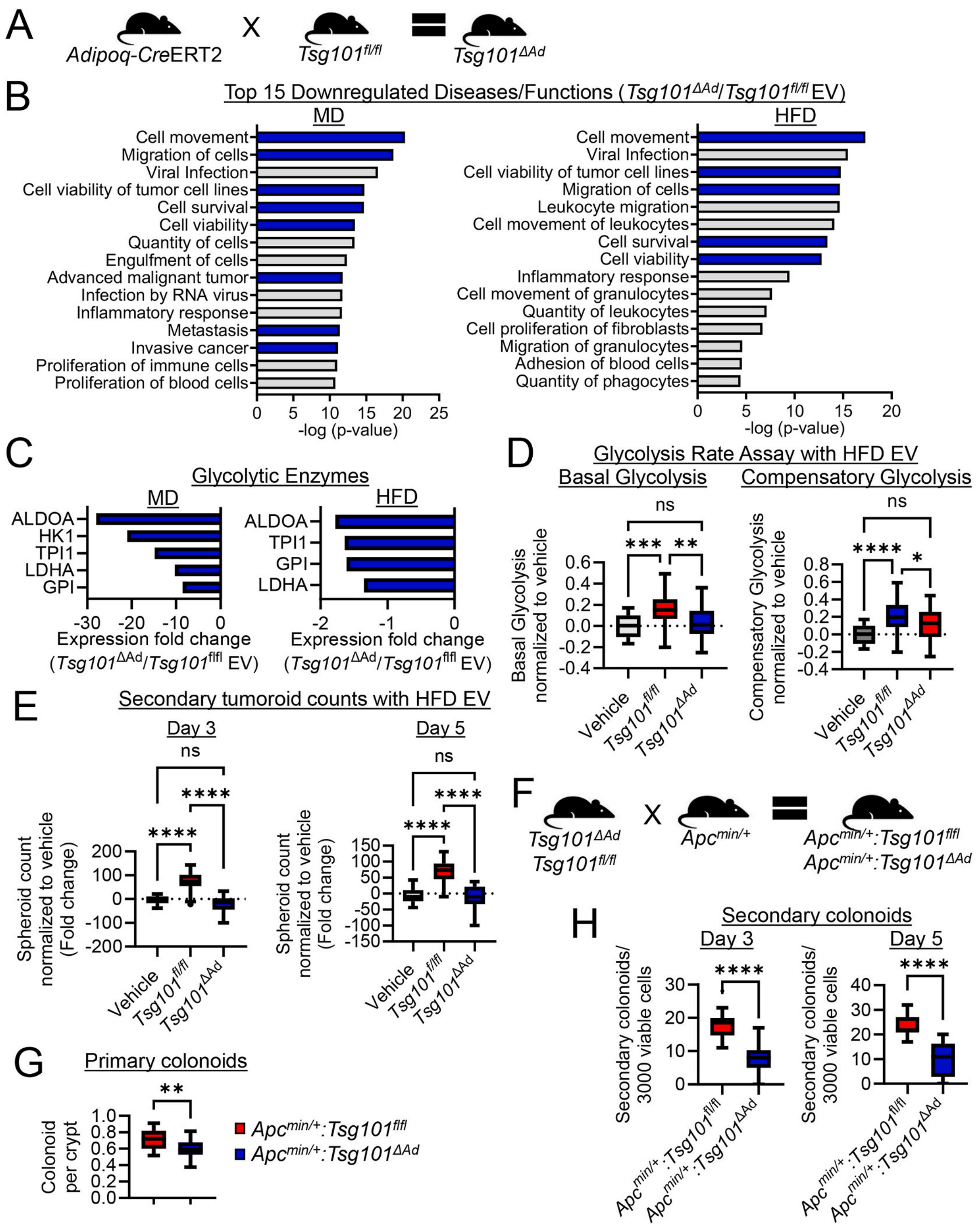

Fig. 5. ***Tsg101*$^{\Delta Ad}$ mice secrete EVs with altered proteome and function.** (A) Schematic diagram of generation of *Tsg101*$^{\Delta Ad}$ mice. (B) Unbiased proteomics was conducted on MD or HFD-fed *Tsg101*$^{\Delta Ad}$ *and Tsg101*^{flfl} -derived VAT EVs and data was analyzed by IPA analysis. Top 15 downregulated diseases/functions in *Tsg101*$^{\Delta Ad}$ mice-derived EVs compared to *Tsg101*^{flfl} -derived EVs across both diets. (C) Downregulation of glycolytic enzymes in *Tsg101*$^{\Delta Ad}$ mice-derived EVs compared to *Tsg101*^{flfl} -derived EVs across both diets. (D) Seahorse XF real-time Glycolytic rate analysis of MC-38 cells. Basal and compensatory glycolysis of MC-38 cells after 24 h treatment with vehicle, *Tsg101*^{flfl} or *Tsg101*$^{\Delta Ad}$ mice-derived EVs. Data is presented as mean of three independent experiments. (E) *Apc*$^{min/+}$ tumoroids were treated with vehicle, *Tsg101*^{flfl} or *Tsg101*$^{\Delta Ad}$ mice-derived EVs on alternate days and secondary tumoroids were established on day 4. Data is presented as mean of three independent experiments. (F) Schematic diagram of generation of *Apc*$^{min/+}$*:Tsg101*$^{\Delta Ad}$ mice. (G) Colonoids generated per crypt from HFD-fed *Apc*$^{min/+}$*: Tsg101*^{flfl} and *Apc*$^{min/+}$*:Tsg101*$^{\Delta Ad}$ mice on day 4 of culture; n = 3 mice each group. (H) Number of secondary colonoids formed per well of 3000 viable single cells of primary colonoids after 4 days of culture; n = 3 mice each group. Data were analyzed by one-way ANOVA with Tukey's posthoc analysis (D, E) or unpaired *t*-test (G, H), $^{*}p < 0.05$, $^{**}\leq 0.01$, $^{***}\leq 0.001$, $^{****}\leq 0.0001$, ns = not significant.

12.5 %), a trend also observed in MD fed mice (11 vs 0 %) (Fig. 6C). Interestingly, 45 % of *Apc*$^{min/+}$*:Tsg101*$^{\Delta Ad}$ mice fed HFD exhibited normal histological scoring as compared to only 20 % of *Apc*$^{min/+}$*: Tsg101*^{flfl} mice fed HFD (Fig. 6C). Additionally, proliferation within colonic polyps was not altered between genotypes, which agreed with our *in vitro* proliferation data in HCT-116 cells (Fig. 6D, E, S4). On the other hand, we observed that in normal colonic crypts, HFD-fed *Apc*$^{min/+}$*:Tsg101*$^{\Delta Ad}$ mice had reduced proliferative capacity compared to *Apc*$^{min/+}$*:Tsg101*^{flfl} mice (Fig. 6F and G). Collectively, these results suggest that during *Apc*-deficiency, VAT-derived EVs under the influence of HFD enhance intestinal crypt proliferation, dysplasia initiation, and dysplastic progression.

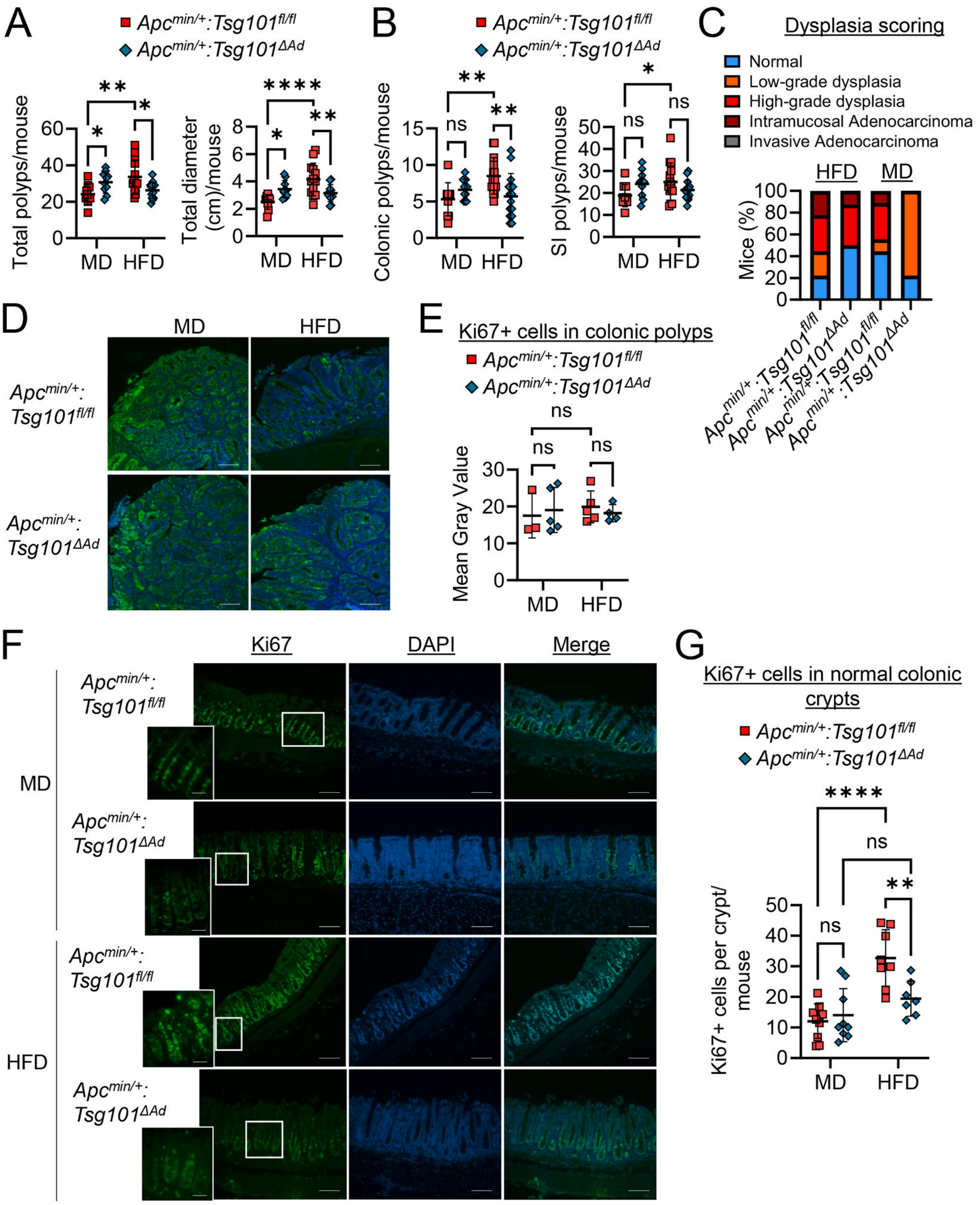

Fig. 6. ***Apc***$^{min/+}$***:Tsg101***$^{\Delta Ad}$ **mice on HFD have reduced colonic polyp formation.** (A) Total (colonic and small intestinal) polyp counts (left) and polyp size (summation of diameters) (right) per mouse of *Apc*$^{min/+}$*:Tsg101*$^{fl/fl}$ and *Apc*$^{min/+}$*:Tsg101*$^{\Delta Ad}$ mice-fed MD (n = 10/genotype) or HFD (n = 14/genotype) for 13 weeks. (B) Colonic (left) or small intestine (right) polyp counts per mouse of *Apc*$^{min/+}$*:Tsg101*$^{fl/fl}$ and *Apc*$^{min/+}$*:Tsg101*$^{\Delta Ad}$ mice-fed MD or HFD for 13 weeks. (C) Percentage of mice displaying highest extent of dysplasia in MD (n = 9/genotype) or HFD (n = 9, *Apc*$^{min/+}$*:Tsg101*$^{fl/fl}$ or n = 8, *Apc*$^{min/+}$*:Tsg101*$^{\Delta Ad}$). (D) Immunofluorescent staining of colonic polyps for Ki67 from HFD-fed mice. (E) Immunofluorescent intensity of Ki67+ cells in colonic polyps was visualized under the microscope. Bar = 300 μm (F) Immunofluorescent intensity of normal crypts for Ki67 was measured by ImageJ; n = 3–5 mice per genotype. Bar = 300 μm, inset bar = 50 μm (G) Number of Ki67+ cells per crypt per mouse was quantitated using Zeiss microscope; n = 8–10 mice per genotype.

3. Discussion

Obesity increases the risk of CRC by 36 %, with men at a slightly higher risk than women [46]. Obesity-associated inflammation in VAT, increased secretion of adipokines, altered gut microbiome and systemic metabolic syndrome have been associated with promoting tumorigenesis [16,47]. In particular, the dysregulation of VAT secretome in obesity has been found to contribute to tumorigenesis by increasing stem-like ability of cancer cells [19,25] and enhancing their metabolic activity [18]. Here, we identify VAT-derived EVs as key signaling mediators between VAT and CRC cells, providing evidence of their role in regulating CRC metabolism, stem-like ability, and tumor development.

Cellular metabolism regulates neoplastic transformation of ISCs and adenoma-to-carcinoma progression in early stages of CRC. ISCs [48] and human colonic adenomas [49] express low levels of mitochondrial pyruvate carrier (MPC) which routes pyruvate into mitochondria for oxidative phosphorylation. This low MPC expression promoted a glycolytic signature and increased stem cell gene expression in AOM-DSS and *Apc* knockout mouse models of CRC [49]. Furthermore, CRC stem cells upregulated glycolysis to lower cellular ROS for maintaining self-renewal capacity and to gain an invasive phenotype [50]. These studies highlight the essential role of glycolysis in CRC tumorigenesis and colonic stem cell maintenance. Our data demonstrates that during obesity, human and mouse VAT-derived OB EVs are enriched in glycolytic enzymes. Using TPI1 as a marker of glycolytic enzymes packaged within EVs, we observed OB EVs induced an upregulation in TPI1 levels and an exacerbation of glycolysis in CRC cells compared to N-OB EVs. This is in agreement with a recent study which identified increased lactate in the serum of CRC patients with obesity compared to normal-weighted CRC patients [51], indicating an upregulation in glycolysis in clinical settings. Moreover, in melanoma, adipocyte-EVs altered cancer metabolism and supported growth by transferring metabolic enzymes [18] or metabolites [43] to melanoma cells. Obese breast adipose tissue-derived EVs increased OxPhos and proliferation of breast cancer cells due to an enrichment of oncogenic miRNA [52]. Interestingly, OB EVs did not increase TPI1 mRNA expression in recipient CRC cells, suggesting a lack of endogenous upregulation nor delivery of TPI1 mRNA as cargo by OB EVs. Therefore, we conclude that the increase in glycolysis may be associated with exogenous transfer of increased TPI1 protein packaged in OB EVs to CRC cells and future studies will test this. An increase in glycolysis could also be observed due to increased metabolites transported within the cell by glucose transporters [53] or from EV cargo. Future studies will focus on interrogating the metabolite profile of EV cargo and EV-treated CRC cells.

Multiple studies have demonstrated that HFD-induced obesity increased ISC proliferation, survival and accelerated intestinal tumorigenesis [12,13,24]. In the setting of wild-type *Apc*, we recently demonstrated that OB EVs acetylate β-catenin in the WNT/β-catenin pathway, a canonical regulator of ISC self-renewal and maintenance. This resulted in the upregulation of *Wnt* target genes and was associated with an elevation in non-transformed ISC stemness [24]. Building upon our previous work, we now demonstrate that OB EVs increase stem-like characteristics and self-renewal capacity of established CRC cells in multiple *in vitro* models harboring aberrant WNT activation, including HCT-116 CRC cells and tumoroids derived from *Apc*$^{min/+}$mice. We also demonstrate that this is associated with OB EV-induced upregulation of glycolysis, that is acquired by and linked to survival of CRC stem-like cells [49,54]. Previous studies reported WNT signaling in CRC as an activator of glycolysis via transcriptional upregulation of key glycolytic enzymes [55,56]. Our studies suggest further enhancement of glycolysis during aberrant WNT-driven CRC by OB EVs. Future work will assess OB EV-induced metabolism and stemness response in CRCs not driven by early aberrant WNT activation, such as in microsatellite instability-high (MSI-high) CRC that is driven by *BRAF* mutations [9,10]. Interestingly, single-cell resolution atlas of human colorectal polyps identified distinct paths for pre-cancer-to-cancer transformation, with MSI-high arising from metaplasia of differentiated cells versus MSS CRCs derived from stem cell expansion [57]. Obesity is more highly associated with MSS CRC versus MSI-high CRC, similar to normal weight patients [58,59] and high BMI is associated with CRC with increased WNT signaling [60]. However, CRC patients with obesity have similar rates of *APC* mutations [60,61] and *BRAF* mutations [62–64] as those with normal weight, suggesting that obesity is likely not the cause of initiating driver mutations, but may promote progression to tumorigenesis after the mutation is present. Ongoing studies will determine obese VAT EVs influence on tumor progression in CRCs harboring different driver mutations.

EV biogenesis involves formation of endosomes from plasma membrane invagination, sorting of specific cargo within EVs and secretion from the parent cells. This step-by-step process is conducted by ESCRT proteins, among which is the scaffolding protein, Tsg101. Tsg101 can recognize ubiquitinated proteins within the cell and helps to sort cargo within EVs [30]. It also interacts with arrestin domain-containing protein 1 (ARRDC1) to release EVs through direct budding from the plasma membrane, which has a different cargo composition than endosomal EVs [65]. To model the impact of VAT EVs and cargo in *in vivo*, we generated *Tsg101*$^{\Delta Ad}$ mice with an altered proteomic cargo and observed a specific downregulation of glycolytic enzymes. Accordingly, we demonstrate that *Tsg101*$^{\Delta Ad}$-EVs protect against HFD-induced upregulation of glycolysis and stem-like properties. *In vivo*, *Apc*$^{min/+}$*:Tsg101*$^{\Delta Ad}$ were protected against HFD-induced polyp formation and increased proliferation of normal colonic crypts. The observed pro-tumorigenic effect of VAT-derived OB EVs can also be mediated through EV interaction with other components in the tumor microenvironment, for instance immune cells or gut microbiota. Although we previously reported that *in vivo* OB EVs in the systemic circulation are taken up by the colon [24], we did not identify the recipient cell type. Therefore, future studies will focus on exploring OB EV uptake and its impact on non-CRC cells in the tumor microenvironment to further elucidate the crosstalk between VAT-derived EVs and CRC tumors.

A limitation of our current study is the difficulty in obtaining pure EV preparations with ultracentrifugation. Although our initial spin removed any large bodies, our EV preps can potentially contain protein aggregates, non-vesicular particles [66] or lipoproteins [67]. However, our NTA and TEM (Fig. 1B and C) demonstrate that our samples are enriched for vesicles ranging from the size 50–350 nm that express common EV markers (Fig. 1D). Nonetheless we cannot exclude protein aggregates or non-vesicular entities from our preps and this could confound our results. For instance, the observed increase in TPI1 (Fig. 3E) could be mediated through transfer of enzymes from protein aggregates or non-vesicular entities rather than EV cargo. However, we subsequently isolated EVs through SEC which is known to separate EVs from protein aggregates, non-vesicular particle and reduce lipoproteins [39,40] and confirmed that such contaminants do not confound our observed results (Fig. S2A and S2B). Another limitation in the study is the lack of information on the fat content of patient's diets used in this study, but several reports based on US data sets have demonstrated that increased fat consumption is a major driver of obesity in this country [68]. While our study focused on HFD-induced obesity, fructose-rich diets have also been implicated in development of obesity [69] and EV-mediated effects under high-fructose diet needs to be evaluated. Another limitation is that the analysis of EV secreted from VAT altered by only one mouse model of obesity driven by HFD. In addition to diet-induced obesity, future studies will determine the influence of VAT EVs on CRC using additional genetic mouse models of obesity. The *Apc*$^{min/+}$ model mainly develop small intestinal polyps compared to the colon; but when challenged with HFD, exhibit colonic adenocarcinoma [14]. Nevertheless, the impact of OB EVs in a CRC mouse model that predominantly develop colonic adenocarcinoma with minimal small intestinal tumors [70] will be investigated in the future.

In summary, our results demonstrate that during obesity, VAT-derived EVs communicate with CRC cells to alter their metabolism, gain stem-like abilities *in vitro* and increase polyp formation *in vivo*. Our study provides compelling evidence that HFD-induced intestinal tumorigenesis is in part mediated by VAT-derived OB EVs and its proteomic cargo. Future studies will focus on studying EV cargo alteration in terms of miRNA and DNA in the background *Tsg101* knockout to elucidate a holistic understanding of EV-mediated effects on CRC development.

4. Materials and methods

Cell lines. Human CRC cell lines HCT-116 (ATCC, US) and HT-29 (ATCC, US) were cultured in Dulbecco's Modified Eagle Medium (DMEM) and Roswell Park Memorial Institute Medium (RPMI), respectively, supplemented with 10 % fetal bovine serum (FBS, Cancer Center Cell Technologies Shared Resource, University of Colorado Anschutz Medical Campus, 89510-186) and 1 % penicillin/streptomycin (P/S, Sigma P4458-100 ML). Murine CRC cell line MC-38 (Kerafast, US) cells were cultured in DMEM supplemented with 10 % FBS, 2 mM L-glutamine, 0.1 mM nonessential amino acids, 1 mM sodium pyruvate, 10 mM HEPES and 1 % P/S. All cell lines were cultured in 10 % exosome-depleted FBS (Gibco, A2720803) during treatment with EVs. Cells were passaged upon reaching 70–80 % confluency. All cell lines were tested for mycoplasma every 8–12 weeks and authenticated by ATCC.

Human adipose tissue and EV isolation. Fresh VAT was obtained from patients with obesity (BMI>30) or non-obese (BMI<30) from Baylor University Medical Center in Dallas, Texas (IRB# 017–254) and approved for secondary research by University of Colorado Anschutz Medical Campus (IRB# 21–4277) and Donor Alliance Organ & Tissue Donation (IRB: 21–4748). The VAT was transported in M199 media, rinsed twice with ice-cold HBSS and then cut into pieces approximately 3–5 mm in diameter with a sterile razor blade. Human VAT was cultured *ex vivo* in approximately 40 ml of DMEM/F12 media (Gibco 11330032) supplemented with PIA Adenosine (100 nM, P4532-25 MG Sigma) for a total of 48 h. The VAT conditioned media (CM) was collected at 24 h, fresh media was added to the VAT and collected again at 48 h. CM was passed through a 0.2 μm filter and stored at −80 °C until further processing. To isolate EVs, VAT CM was subjected to an initial spin at 3,000 g for 15 min. EV pellet was obtained by ultracentrifugation of supernatant at 100,000 g for 90 min (Beckman Coulter, SW 41 Ti swinging bucket rotor) and resuspended in 1x PBS. In the case of fluorescent labeling of EVs, pelleted EVs were incubated with 1 μM 1,1′-Dioctadecyl-3,3,3′,3′-tetramethylindocarbocyanine perchlorate (Dil) dye (Invitrogen, D282) for fluorescence microscopy for 15 min in the dark, washed with 14 ml 1x PBS and pelleted at 100,000 g again for 90 min. These ultracentrifugation-isolated EVs were further subjected to 35 nm qEV SEC-columns (ICO-35, iZON Science) and eluted with PBS. Eluted fractions 5–10 were found to contain highest numbers of EVs by NTA and were subsequently pooled for experiments pertaining to Western blot of TPI1. EVs were aliquoted and stored at −80 °C until use [71].

Dietary model of obesity. C57BL/6 J wild-type mice were fed a purified Western diet consisting of 45 % kcal fat (HFD; Research Diets D12451) or 10 % kcal fat (MD; Research Diets D12450H) *ad libitum* beginning at weaning (3–4 weeks of age) for 16 weeks. Body weight was measured weekly. All mice were grouped-housed in standard cages under specific pathogen-free conditions and were allowed standard tap water *ad libitum.* All experiments were approved by the University of Colorado and the Veterans Affairs Institutional Animal Care and Use Committees.

Mouse adipose tissue and EV isolation. VAT (perigonadal, perirenal, retroperitoneal, and mesenteric) was isolated from HFD- or MD-fed mice. VAT from different depots were combined, rinsed twice with ice-cold HBSS and all visible blood vessels or hair were dissected and removed. VAT was cut into pieces approximately 3–5 mm in diameter with a sterile razor blade. At least 1 g VAT was used for *ex vivo* culturing in approximately 12 ml DMEM/F12 media supplemented with PIA Adenosine (100 nM, P4532-25 MG Sigma) for a total of 48 h. Unlabeled and labeled EVs from VAT-CM was isolated through ultracentrifugation as human EVs.

Transgenic mouse models. All experiments were approved by the University of Colorado and the Veterans Affairs Institutional Animal Care and Use Committees. *Tsg101*$^{fl/fl}$ mice (FVB background) were purchased from the Mutant Mouse Resource and Research Center (MMRRC, stock no. 037407-MU; supported by the Office of Infrastructure Development Programs, National Institutes of Health; Bethesda, MA, USA). *Tsg101* mutant mice were generated by flanking exon 1 of the *Tsg101* gene with loxP sites [72]. *Tsg101*$^{fl/fl}$ mice were backcrossed with C57BL/6 J mice (The Jackson Laboratory, stock 000664, Farmington, CT, USA) for 7 generations prior to experimentation. Genetic monitoring was conducted (Transnetyx Inc., TN, USA) to ensure successful backcrossing. *Tsg101*$^{fl/fl}$ mice were crossed with *Adiponectin-Cre-ER*^{T2} mice (The Jackson Laboratory, stock 025124; C57BL/6 J). We crossed the resulting offspring with *Apc*$^{min/+}$ (The Jackson Laboratory, stock 002020; C57BL/6 J) which is common model for intestinal tumorigenesis [43,70]. The resulting offspring were genotyped by PCR analysis of tail genomic DNA obtained at weaning for expression of the floxed *Tsg101* allele using primer sequences previously described [72] and *Adipnectin-Cre-ER*^{T2} transgene using 5′-CCGCATCTTCTTGTGCAGT-3′ (Internal Positive Control Forward), 5′-ATCACGTCCTCCATCATCC-3′ (Internal Positive Control Reverse), 5′-GAGTCTGCCTTTCCCATGAC-3′ (Transgene Forward), and 5′-TCCCTCACATCCTCAGGTT-3′ (Transgene Reverse) sequences and *Apc*$^{min/+}$ mutation using 5′- GCC ATC CCT TCA CGT TAG-3′ (wild type), 5′-TTC CAC TTT GGC ATA AGG C-3′ (Common) and 5′-TTC TGA GAA AGA CAG AAG TTA-3′ (Mutant) as specified by Jackson Laboratories. Experiments were performed with age- and gender-matched littermate mice. All mice were grouped-housed in standard cages under SPF conditions and were allowed standard chow and tap water *ad libitum.* For dietary obesity studies, MD or HFD feeding was performed as described for wild-type mice above. To induce *Tsg101* deletion in *Apc*$^{min/+:}$*Tsg101*$^{\Delta Ad}$*,* 100 μl of 10 mg/ml tamoxifen was intraperitoneally (i.p.) injected at 6 weeks of age for 4 consecutive days and repeated every 4 weeks to maintain deletion. Similarly, *Apc*-$^{min/+:}$*Tsg101*^{flfl} mice were also injected with the same dose of tamoxifen as control.

Nanoparticle tracking analysis (NTA). EV particle number and size was measured by NTA using NanoSight (NanoSight NS300; Malvern Panalytical). EVs were diluted 1:10 or 1:100 in ddH$_2$0, injected into the NanoSight sample port using a syringe and analyzed using a camera level of 7 and detection threshold of 5 at 22 °C.

Transmission electron microscopy (TEM). A 10 μl drop of EV sample was applied to a freshly glow-discharged 300 mesh formvar and carbon coated grid (Electron Microscopy Sciences) for 5 min and blotted with filter paper. The grid was then washed one time by applying 10 μl water on the grid and blotted with a Whatman filter paper. Finally, the grids were stained with 10 μl of 2 % uranyl acetate solution. After blotting, the grids were allowed to dry. Samples were imaged on a Tecnai G2 Biotwin TEM (Thermo Fisher) at 120 kV with an AMT low mount NS15B sCMOS camera (AMT Imaging).

Confocal Microscopy. HCT-116 cells were treated with Dil-labeled N-OB or OB EVs at 10^7 EV particles/ml for 24 h. To remove non-internalized/bound EVs, cells were washed twice with 1x PBS and 30 min prior to imaging, Cell Mask Plasma Membrane Stain (Invitrogen, C37608) was added at 1:150 dilution. Cells were incubated for 15 min at 37 °C. Cells were washed three times with 1x PBS to remove excess dye. Fluorescent signal was imaged at 40X through Z-stack of cells by an inverted laser scanning confocal microscope, Zeiss LSM780.

Mass spectrometry and proteomic analysis. Isolated EVs from VAT-CM of 3 non-obese (BMI<30) and 3 obese (BMI>30) patients were lysed using 10X cell lysis buffer (9803 S, Cell Signaling) for 10 min on ice. Protein content was measured using Bradford Assay and 10 μg protein was submitted to Mass Spectrometry Proteomics Shared Resource Facility at the University of Colorado Anschutz Medical Campus. In brief, Samples were subjected to proteolytic digestion using a filter-aided sample preparation (FASP) protocol with 10 kDa molecular weight cutoff filters (Sartorius Vivacon 500 #VN01H02). Samples were reduced with 5 mM tris (2-carboxyethyl phosphine), alkylated with 50 mM 2-chloroacetamide, and digested overnight with trypsin (enzyme:substrate ratio 1:50) at 37 °C. Peptides were recovered from the filter using successive washes with 0.2 % formic acid (FA). Aliquots containing 10 μg of digested peptides were cleaned using PierceTM C18 Spin Tips (Thermo Scientific) according to the manufacturer's protocol, dried in a vacuum centrifuge, and resuspended in 0.1 % FA in mass spectrometry-grade water.

Liquid chromatography mass spectrometry (LC-MS/MS) was performed using an Easy nLC 1000 instrument coupled to a Q Exactive™ HF Mass Spectrometer (both from ThermoFisher Scientific). Peptides were loaded on a C18 column (100 μM inner diameter x 20 cm) packed in-house with 2.7 μm Cortecs C18 resin, and separated at a flow rate of 0.4 μl/min with solution A (0.1 % FA) and solution B (0.1 % FA in acetonitrile) and under the following conditions: isocratic at 4 % B for 3 min, followed by 4 %–32 % B for 102 min, 32 %–55 % B for 5 min, 55 %–95 % B for 1 min and isocratic at 95 % B for 9 min. The mass spectrometer was operated in data-dependent acquisition (DDA) mode with the top 15 most abundant precursors being selected for MS/MS analysis.

Fragmentation spectra were searched against the UniProt mouse proteome database (Proteome ID # UP000000589) using the MSFragger-based FragPipe computational platform [73]. Contaminants and reverse decoys and were added to the database automatically. The precursor-ion mass tolerance and fragment-ion mass tolerance were set to 10 ppm and 0.2 Da, respectively. Fixed modifications were set as carbamidomethyl (C), and variable modifications were set as oxidation (M) and two missed tryptic cleavages were allowed, and the protein-level false discovery rate (FDR) was ≤ 1 %. Final analysis was conducted with proteins with ≥ 10 spectral using Panther Pathway database analysis [74] and QIAGEN Ingenuity Pathway Analysis (QIAGEN IPA). Protein pathways/function with a p-value <0.05 and z-score >2 were considered as differentially expressed pathways/function.

RNA sequencing. HCT-116 cells were treated with vehicle, N-OB and OB EV at 10ˆ7 EV particles/ml for two consecutive days. Cells were harvested for RNA isolation using RNeasy® Mini Kit (Qiagen) and on-column DNase treatment. RNA concentration and quality was assessed by microplate reader (BioTek Synergy HTX Multimode Reader, USA). RNA (2 μg) was submitted to Novogene Co., Ltd (CA, USA) for RNA library and transcriptome sequencing.

qRT-PCR. For quantitative real-time PCR analysis, total RNA was isolated using Trizol (Invitrogen) and was transcribed into cDNA using qScript Flex cDNA Synthesis kit (Quantabio). Gene expression analysis was performed using Power SYBR Green Master Mix Assay (Applied Biosystems) on a Step One Plus real-time PCR detection system (Applied Biosystems). β-actin was used as a control and results were calculated using the Δ-ΔCt method. Gene expression analysis using the following primers from Integrated DNA Technologies were performed. Notch 1: 5′-CAGAGTGGACAGGTCAGTA-3’ (Sense); 5′-GACACACACGCAGTTGTA-3’ (AntiSense), Notch 2: 5′-GATGTGCCTCAGGGTTTAC-3′(Sense); 5′-CTTGACAGGTGCACTCATAG - 3’ (AntiSense) and Egfr: 5′-GGTGGTCCTTGGGAATTT - 3’ (Sense); 5’ -TGTGTTGAGGGCAATGAG-3’ (AntiSense).

Western blot analysis. HCT-116 and MC-38 were collected by incubating with lysis (1 mM EDTA, 1 mM Na_3VO_4, 1 mM NaF, 1 % IGPAL, Triton X100) for 10 min on ice and after centrifuging at 500×*g* for 5 min at 4 °C to pellet cell debris. Supernatant was collected for total protein and separated by SDS-PAGE. Human N-OB and OB EVs were lysed with 10X cell lysis buffer to release EV proteins and run on SDS-PAGE. Proteins were transferred to nitrocellulose membrane (BioRad) blocked with 5 % milk and probed with the following primary antibodies: Tsg101 (Santa Cruz Biotechnology, sc-7964; 1:200), CD9 (Invitrogen, MA5-31980, 1:500), Adiponectin (Santa Cruz, sc-136131, 1:200), TPI1 (ProteinTech, 10713-1-AP, 1:1000), and β-actin (Millipore, A1978-200UL, 1:10,000). After incubation with HRP-labeled anti-mouse or anti-rabbit IgG secondary antibody, membranes were incubated with Pierce ECL solution (Thermo Scientific, 32106) for 1–2 min and imaged on BioRad Imager.

ATP rate assay and glycolysis rate assay. Real time ATP production rate and glycolysis rate of CRC cells were quantified using Seahorse XF Real-Time ATP Rate Assay Kit (103592-100) and Glycolytic Rate Assay Kit (103344-100) respectively. In brief, HCT-116, HT-29 or MC-38 cells were shifted to media containing 10 % exosome free FBS (Gibco, A2720803) and treated with vehicle (veh), N-OB or OB EVs at 10ˆ7 (HCT-116) or 10ˆ8 EV (MC-38) particles/ml for 24 h. On the day of the assay, cells were stained with Hoescht 33342 (Sigma) and cell number was counted using Cytation 1 Cell Imaging Multi-ModeReader (BioTek) to normalize seahorse metabolic data. Seahorse metabolic data was recorded in WAVE program (Agilent).

Spheroid formation and limiting dilution assay. HCT-116 cells in monolayer were digested and mechanically dissociated into a single cell suspension followed by passage through a 25-gauge needle. Cells were seeded in 96 well flat-bottomed ultra-low attachment plate (Corning) at 7000 cells/well. Spheroids were grown in stem cell media consisting of DMEM supplemented with 20 ng/ml human EGF, 20 ng/ml bFGF (Gibco, 13256029) and 1x N2 supplement (Gibco, 17502-048). Spheroids were treated with veh, N-OB and OB EV (10^7 EV particles/ml) on the day of plating, day 0 and on day 2. Spheroid number was measured on day 3 and 4 through live-cell imaging by Incucyte (Sartorius) under the multi-spheroid module. For limiting dilution assay, spheroids were seeded and treated as above at limiting cell numbers, 5000, 2500, 1250, 625, 100 and 50 cells and spheroid number was tracked by Incucyte. The frequency of stem cells at limiting dilutions among different groups were analyzed using Extreme Limiting Dilution Analysis web tool [75].

Adenomatous polyp counting and sizing. The entire intestinal tract was removed, divided according to anatomical location (duodenum, jejunum, ileum, and colon) and total adenomatous polyp number was quantitated and largest diameter was measured using a dissecting microscope (LSM-Z220P-LS100, Laxco). Adenomatous polyps were stored in −80 °C for biochemical analysis or whole colonic tissue with polyps were prepared for histologic evaluation.

Colonic adenoma scoring. Hemotoxylin and eosin-stained colon sections were scored histologically for adenocarcinoma (neoplasia). Scoring was performed in a blind fashion by a certified GI pathologist (Dr. David Orlicky). Score was given based on these criteria: normal (score 0), low grade dysplasia (score 1), high grade dysplasia (score 2), intramucosal adenocarcinoma (score 3), and invasive adenocarcinoma (score 4) [76].

***Apc*$^{min/+}$-derived tumoroid formation.** *Apc*$^{min/+}$ mice were sacrificed by CO_2 asphyxiation at 20–24 weeks. Colonic tumors were excised from the colon and placed in 5 ml ice-cold washing medium (DMEM/F-12 Gibco 11330032; HEPES, Gibco 15630-080; L-glutamine, Gibco 25030-081; FBS from Cancer Center Cell Technologies Shared Resource, University of Colorado Anschutz Medical Campus, 89510-186; and P/S, Sigma P4458-100 ML). Tumors were minced with a sterile new blade and digested in 1 ml collagenase solution (washing medium, 75 U/ml Collagenase XI C9407-25 MG, 125 μg/ml Dispase II D4693-1G, 100 μg/ml Primocin, Invivogen NC9141851) for 20–30 min at 37 °C. 4 ml of washing medium and 5 ml of 2 % sorbitol was added to digested biopsies. Tissue digestions were filtered through 70 μm filter to get a single suspension of cells, which was centrifuged at 1500 rpm for 5 min to form a pellet. The pellet was resuspended in 10 μl volume of Matrigel (Corning, CB-40230) and seeded into 48 well plate. Tumoroids were cultured in 250 μl media containing, L-WRN from Organoid and Tissue Modeling Shared Resource core, University of Colorado Anschutz Medical Campus; DMEM/F12 supplemented with FBS, L-glutamine, P/S, Primocin and Y-27632 Sigma, 688000-1 MG. Tumoroid culture media was replaced every 2 days.

***Apc*$^{min/+}$-derived tumoroid treatment and self-renewal assay.** *Apc*$^{min/+}$-derived tumoroids were moved to ERN differentiation media supplemented with 20 ng/ul recombinant mouse Wnt3α (1324-WN-002, R&D Systems). ERN media is composed of DMEM/F12, Primocin, HEPES, 1X N2 supplement, 1ng/ul EGF, 2 ng/ul Noggin (250-38, PeproTech), 10 ng/μl murine R-spondin (3474-RS-050, R&D Systems). Tumoroids were treated with veh, N-OB and OB EV at 10ˆ7 EV particles/ml on day 0 and day 2. For tumoroid regeneration assay, primary tumoroids were dissociated on day 4 using TrypLE (Gibco, 12605010), counted, and plated at 1000 viable cells/well in fresh Matrigel and tumoroid culture media for secondary tumoroid formation. Secondary tumoroids were visualized, imaged (10X) and counted manually under an inverted microscope (JENCO, USA).

Primary colonic crypt isolation from *Apc*$^{min/+}$:*Tsg101*$^{\Delta Ad}$ mice. Mouse colon crypts were isolated from age and sex-matched *Apc*$^{min/+}$:*Tsg101* $^{fl/fl}$ or *Apc*$^{min/+}$:*Tsg101*$^{\Delta Ad}$ using the method by Sato et al. [8]. Briefly, colons were inverted and incubated in ice-cold 6 mM EDTA solution for 40 min with gentle rocking. Next, colonic crypts were separated from colonic tissue through gentle shaking by hand, visualized under inverted microscope, and embedded in Reduced Growth Factor Matrigel (356230, BD Biosciences). Colonoids were cultured in WERN media: Advanced DMEM/F-12 (Gibco, 12634-010, ThermoFisher) supplemented with GlutaMAX (Gibco 35050-061, ThermoFisher), Primocin, HEPES, 1 × N2 supplement, 1 ng/µl EGF (2028-EG, R&D Systems), 2 ng/µl Noggin (250-38, PeproTech), 10 ng/µl murine R-spondin (3474-RS-050, R&D Systems), and Y27632. Complete WENR organoid media was obtained from the Organoid and Tissue Modeling Shared Resource core, University of Colorado Anschutz Medical Campus. Colonoid culture media was replaced every 48 h. Primary tumoroids were visualized, imaged (10X) and counted manually under an inverted microscope.

Immunofluorescence. Colonic tissue was fixed in 10 % formalin and embedded in paraffin. 7 µm paraffin-embedded sections of mouse or human ileum were dehydrated in xylene and ethyl alcohol gradient, incubated in 10 mM sodium citrate for antigen epitope retrieval, blocked in 5 % normal donkey serum, and exposed to the following primary antibody at 4 °C overnight: Ki67 (anti-rat, 1:100, 14-5698-82, eBioscience). Next day, tissues were washed with 1x PBS and incubated with secondary antibody (Goat anti-Rat IgG Secondary Antibody at 1:250, A-11006, Invitrogen). Sections were then stained with 4′,6-Diamidino-2-phenylindole dihydrochloride (DAPI, D9542, Sigma) at 1:1000 in 1 × PBS for 1 min. Polyp sections were visualized using Zeiss at 10x and 40x (for Ki67$^+$ cell counting). Ki67 intensity was measured by ImageJ.

Cell Counting Kit 8 proliferation assay. Cell proliferation of live HCT-116 cells were tested with Cell Counting Kit 8 (Abcam, 228554). 20 µl of WST-8 solution was added per well and mixed gently. The cells were incubated in the dark at 37°C and then absorbance was measured at 460 nm with a BioTek Synergy HTX microplate reader.

cBioPortal for Cancer Genomics analysis. The colorectal adenocarcinoma dataset from PanCancer Atlas (TCGA; $n = 594$ samples) was analyzed using the cBioPortal platform (https://www.cbioportal.org/) to assess protein expression of TPI1. Kaplan-Meier survival plot of TPI1 protein high ($N = 44$) and low ($N = 550$) patients was generated from cBioPortal platform.

Statistical analysis. All data with two test-groups were normally distributed and analyzed using unpaired 2-tailed Student's t-test for single comparisons. For data with more than two test-groups, normally distributed data was tested with 1-way or 2-way ANOVA with Tukey's post-hoc test and for data without normal distribution, Kruskal-Wallis test with Dunn's post-hoc test for multiple comparisons was used (PRISM 6.0, GraphPad Software). Outliers were identified by Grubb's test ($\alpha = 0.05$) and removed as appropriate. $P < 0.05$ was considered significant.

CRediT authorship contribution statement

Parsa S. Haque: Writing – review & editing, Writing – original draft, Investigation, Funding acquisition, Formal analysis, Data curation, Conceptualization. **Sheré L. Paris:** Writing – review & editing, Data curation. **Rhonda F. Souza:** Writing – review & editing, Conceptualization. **Joseph C. Onyiah:** Writing – review & editing, Data curation. **Christina Coughlan:** Writing – review & editing, Data curation. **David J. Orlicky:** Writing – review & editing, Formal analysis. **Janos Zempleni:** Writing – review & editing, Formal analysis, Conceptualization. **Arianne L. Theiss:** Writing – review & editing, Writing – original draft, Investigation, Funding acquisition, Formal analysis, Conceptualization.

Ethics approval and consent to participate

All mouse experiments were approved by the University of Colorado Anschutz Medical Campus Institutional Animal Care and Use Committee.

Consent for publication

All authors give consent to publish and agree on the final manuscript submission.

Availability of data and materials

The proteomic raw data have been deposited in the PRIDE database http://www.ebi.ac.uk/pride under project PXD061988. RNA sequencing raw and processed data have been deposited in Gene Expression Omnibus under project accession number GSE291093.

Funding

This work was supported by Veteran's Affairs BLRD MERIT IBX005288 (ALT), National Institutes of Health 1F99CA294247 (PSH), Crohn's Colitis Foundation SRA 900820 (ALT), GI & Liver Innate Immune Program (GALIIP) – University of Colorado Anschutz AWD63501470 (ALT).

Declaration of competing interest

The authors declare that they have no known competing financial interests or personal relationships that could have appeared to influence the work reported in this paper.

Acknowledgements

We thank the University of Colorado Alzheimer's and Cognition Center and Exosome Core for assistance with NTA. We thank Dr. Anthony Saviola in the Mass Spectrometry Proteomics Shared Resource Facility (National Institutes of Health - P30CA06934) at University of Colorado Anschutz Medical campus for assistance with proteomic analysis. We thank Dr. Matthew Jackman in the Mitochondrial Sub Core, Nutrition Obesity Research Center (National Institutes of Health -P30DK048520), at University of Colorado Anschutz Medical campus for assistance with Seahorse analysis. We acknowledge the use of research samples collected by the Donor Alliance Organ & Tissue Donation and provided to us by the Pathology Shared Resource located at the University of Colorado Anschutz Medical Campus (RRID: 021989). These samples were an integral part of the study and contributed to our findings, and we appreciate their willingness to share these valuable resources. We would like to thank Drs. Benjamin Bitler and Ritsuko Iwanaga, University of Colorado Anschutz Medical Campus, for providing their expertise on extreme limiting dilution assay.

Appendix A. Supplementary data

Supplementary data to this article can be found online at https://doi.org/10.1016/j.canlet.2025.218104.

References

[1] R.L. Siegel, T.B. Kratzer, A.N. Giaquinto, H. Sung, A. Jemal, Cancer statistics, CA Cancer J. Clin. 75 (1) (2025) 10–45, 2025.

[2] S. Pati, W. Irfan, A. Jameel, S. Ahmed, R.K. Shahid, Obesity and cancer: a current overview of epidemiology, pathogenesis, outcomes, and management, Cancers (Basel) 15 (2) (2023) 485.

[3] Y.N. Liu, J.F. Gu, J. Zhang, D.Y. Xing, G.Q. Wang, Bariatric surgery reduces colorectal cancer incidence in Obese individuals: systematic review and meta-analysis, World J. Gastrointest. Surg. 15 (10) (2023) 2331–2342.

[4] A. Chierici, P. Amoretti, C. Drai, S. De Fatico, J. Barriere, L. Schiavo, et al., Does bariatric surgery reduce the risk of colorectal cancer in individuals with morbid obesity? A systematic review and meta-analysis, Nutrients 15 (2) (2023).

[5] A. Goyal, C.A. Macias, M.P. Corzo, D. Tomey, S. Shetty, V. Peña, et al., Outcomes of metabolic and bariatric surgery in populations with obesity and their risk of developing colorectal cancer: where do we stand? An umbrella review on behalf of TROGSS—The robotic global surgical society, Cancers (Basel) 17 (4) (2025) 670.

[6] B. Guiu, J.M. Petit, F. Bonnetain, S. Ladoire, S. Guiu, J.-P. Cercueil, et al., Visceral fat area is an independent predictive biomarker of outcome after first-line bevacizumab-based treatment in metastatic colorectal cancer, Gut 59 (3) (2010) 341–347.

[7] G. Xiao, Y. Zheng, H. Chen, M. Luo, C. Yang, D. Ren, et al., Single-cell transcriptome analysis reveals immunosuppressive landscape in overweight and Obese colorectal cancer, J. Transl. Med. 22 (1) (2024) 134.

[8] T. Sato, R.G. Vries, H.J. Snippert, M. van de Wetering, N. Barker, D.E. Stange, et al., Single Lgr5 stem cells build crypt-villus structures in vitro without a mesenchymal niche, Nature 459 (7244) (2009) 262–265.

[9] N. Barker, R.A. Ridgway, J.H. Van Es, M. Van De Wetering, H. Begthel, M. Van Den Born, et al., Crypt stem cells as the cells-of-origin of intestinal cancer, Nature 457 (7229) (2009) 608–611.

[10] E.I. Lin, L.H. Tseng, C.D. Gocke, S. Reil, D.T. Le, N.S. Azad, et al., Mutational profiling of colorectal cancers with microsatellite instability, Oncotarget 6 (39) (2015) 42334–42344.

[11] T. Fu, S. Coulter, E. Yoshihara, T.G. Oh, S. Fang, F. Cayabyab, et al., FXR regulates intestinal cancer stem cell proliferation, Cell 176 (5) (2019), 1098-112.e18.

[12] S. Beyaz, M.D. Mana, J. Roper, D. Kedrin, A. Saadatpour, S.J. Hong, et al., High-fat diet enhances stemness and tumorigenicity of intestinal progenitors, Nature 531 (7592) (2016) 53–58.

[13] M.D. Mana, A.M. Hussey, C.N. Tzouanas, S. Imada, Y. Barrera Millan, D. Bahceci, et al., High-fat diet-activated fatty acid oxidation mediates intestinal stemness and tumorigenicity, Cell Rep. 35 (10) (2021) 109212.

[14] J. Yang, H. Wei, Y. Zhou, C.H. Szeto, C. Li, Y. Lin, et al., High-fat diet promotes colorectal tumorigenesis through modulating gut microbiota and metabolites, Gastroenterology 162 (1) (2022) 135–149 e2.

[15] T.-Y. Kim, S. Kim, Y. Kim, Y.-S. Lee, S. Lee, S.-H. Lee, et al., A high-fat diet activates the BAs-FXR axis and triggers cancer-associated fibroblast properties in the Colon, Cell. Mol. Gastroenterol. Hepatol. 13 (4) (2022) 1141–1159.

[16] B.H.L. Harris, V.M. Macaulay, D.A. Harris, P. Klenerman, F. Karpe, S.R. Lord, et al., Obesity: a perfect storm for carcinogenesis, Cancer Metastasis Rev. 41 (3) (2022) 491–515.

[17] F.Y. Tang, M.H. Pai, E.P. Chiang, Consumption of high-fat diet induces tumor progression and epithelial-mesenchymal transition of colorectal cancer in a mouse xenograft model, J. Nutr. Biochem. 23 (10) (2012) 1302–1313.

[18] E. Clement, I. Lazar, C. Attané, L. Carrié, S. Dauvillier, M. Ducoux-Petit, et al., Adipocyte extracellular vesicles carry enzymes and fatty acids that stimulate mitochondrial metabolism and remodeling in tumor cells, The EMBO journal 39 (3) (2020) e102525.

[19] H. Goto, Y. Shimono, Y. Funakoshi, Y. Imamura, M. Toyoda, N. Kiyota, et al., Adipose-derived stem cells enhance human breast cancer growth and cancer stem cell-like properties through adipsin, Oncogene 38 (6) (2019) 767–779.

[20] J. Bilski, A. Mazur-Bialy, D. Wojcik, M. Surmiak, M. Magierowski, Z. Sliwowski, et al., Role of obesity, mesenteric adipose tissue, and adipokines in inflammatory bowel diseases, Biomolecules 9 (12) (2019) 780.

[21] C. Zhou, Y.-Q. Huang, M.-X. Da, W.-L. Jin, F.-H. Zhou, Adipocyte-derived extracellular vesicles: bridging the communications between obesity and tumor microenvironment, Discov. Oncol. 14 (1) (2023) 92.

[22] T. Camino, N. Lago-Baameiro, S.B. Bravo, A. Molares-Vila, A. Sueiro, I. Couto, et al., Human Obese white adipose tissue sheds depot-specific extracellular vesicles and reveals candidate biomarkers for monitoring obesity and its comorbidities, Transl. Res. 239 (2022) 85–102.

[23] H.Y. Kwan, M. Chen, K. Xu, B. Chen, The impact of obesity on adipocyte-derived extracellular vesicles, Cell. Mol. Life Sci. 78 (23) (2021) 7275–7288.

[24] S. Parsa, D.G. Haque, Thor Kuusivuori-Robinson, Christina Coughlan, Yaritza Delgado-Deida, Joseph C. Onyiah, Janos Zempleni, Arianne L. Theiss, Obese adipose tissue extracellular vesicles activate mitochondrial fatty acid beta-oxidation to drive colonic stemness, Cell. Mol. Gastroenterol. Hepatol. (2025).

[25] G. La Camera, L. Gelsomino, R. Malivindi, I. Barone, S. Panza, D. De Rose, et al., Adipocyte-derived extracellular vesicles promote breast cancer cell malignancy through HIF-1α activity, Cancer Lett. 521 (2021) 155–168.

[26] I. Ramos-Andrade, J. Moraes, R.M. Brandão-Costa, S.V. da Silva, A. de Souza, C. da Silva, et al., Obese adipose tissue extracellular vesicles raise breast cancer cell malignancy, Endocr. Relat. Cancer 27 (10) (2020) 571–582.

[27] I. Lazar, E. Clement, L. Carrié, D. Esteve, S. Dauvillier, M. Moutahir, et al., Adipocyte extracellular vesicles decrease p16INK4A in melanoma: an additional link between obesity and cancer, J. Invest. Dermatol. (2022).

[28] M.E. Williams, D. Howard, C. Donnelly, F. Izadi, J.G. Parra, M. Pugh, et al., Adipocyte derived exosomes promote cell invasion and challenge paclitaxel efficacy in ovarian cancer, Cell Commun. Signal. 22 (1) (2024) 443.

[29] P. Liu, S.-J. Sun, Y.-J. Ai, X. Feng, Y.-M. Zheng, Y. Gao, et al., Elevated nuclear localization of glycolytic enzyme TPI1 promotes lung adenocarcinoma and enhances chemoresistance, Cell Death Dis. 13 (3) (2022) 205.

[30] C.A. René, R.J. Parks, Bioengineering extracellular vesicle cargo for optimal therapeutic efficiency, Molecular Therapy - Methods & Clinical Development 32 (2) (2024) 101259.

[31] M.M. Ibrahim, Subcutaneous and visceral adipose tissue: structural and functional differences, Obes. Rev. 11 (1) (2010) 11–18.

[32] E. Willms, C. Cabañas, I. Mäger, M.J.A. Wood, P. Vader, Extracellular vesicle heterogeneity: subpopulations, isolation techniques, and diverse functions in cancer progression, Front. Immunol. 9 (2018).

[33] K.D. Connolly, I.A. Guschina, V. Yeung, A. Clayton, M.S. Draman, C. Von Ruhland, et al., Characterisation of adipocyte-derived extracellular vesicles released pre- and post-adipogenesis, J. Extracell. Vesicles 4 (2015) 29159.

[34] J. Wang, Y. Ji, X. Cao, R. Shi, X. Lu, Y. Wang, et al., Characterization and analysis of extracellular vesicle-derived miRNAs from different adipose tissues in mice, Heliyon 10 (20) (2024) e39149.

[35] Q. Zhang, T. Deng, H. Zhang, D. Zuo, Q. Zhu, M. Bai, et al., Adipocyte-derived exosomal MTTP suppresses ferroptosis and promotes chemoresistance in colorectal cancer, Adv. Sci. (Weinh.) 9 (28) (2022) e2203357.

[36] A. Kasprzak, Insulin-like growth factor 1 (IGF-1) signaling in glucose metabolism in colorectal cancer, Int. J. Mol. Sci. 22 (12) (2021).

[37] C.-C. Lu, P.-Y. Chu, S.-M. Hsia, C.-H. Wu, Y.-T. Tung, G.-C. Yen, Insulin induction instigates cell proliferation and metastasis in human colorectal cancer cells, Int. J. Oncol. 50 (2) (2017) 736–744.

[38] J. Chen, S. Duan, Y. Wang, Y. Ling, X. Hou, S. Zhang, et al., MYG1 drives glycolysis and colorectal cancer development through nuclear-mitochondrial collaboration, Nat. Commun. 15 (1) (2024) 4969.

[39] K. Ekström, R. Crescitelli, H.I. Pétursson, J. Johansson, C. Lässer, R. Olofsson Bagge, Characterization of surface markers on extracellular vesicles isolated from lymphatic exudate from patients with breast cancer, BMC Cancer 22 (1) (2022) 50.

[40] M. Bordas, G. Genard, S. Ohl, M. Nessling, K. Richter, T. Roider, et al., Optimized protocol for isolation of small extracellular vesicles from human and murine lymphoid tissues, Int. J. Mol. Sci. 21 (15) (2020).

[41] M.I. Che, J. Huang, J.S. Hung, Y.C. Lin, M.J. Huang, H.S. Lai, et al., β1, 4-N-acetylgalactosaminyltransferase III modulates cancer stemness through EGFR signaling pathway in Colon cancer cells, Oncotarget 5 (11) (2014) 3673–3684.

[42] C. Li, H.C. Lau, X. Zhang, J. Yu, Mouse models for application in colorectal cancer: understanding the pathogenesis and relevance to the human condition, Biomedicines 10 (7) (2022).

[43] M. Zhang, D. Yang, B. Gold, The adenomatous polyposis coli (APC) mutation spectra in different anatomical regions of the large intestine in colorectal cancer, Mutat. Res. 810 (2018) 1–5.

[44] N. Shussman, S.D. Wexner, Colorectal polyps and polyposis syndromes, Gastroenterol Rep (Oxf). 2 (1) (2014) 1–15.

[45] M.Y. Park, M.Y. Kim, Y.R. Seo, J.S. Kim, M.K. Sung, High-fat diet accelerates intestinal tumorigenesis through disrupting intestinal cell membrane integrity, J. Cancer Prev. 21 (2) (2016) 95–103.

[46] Z. Ungvari, M. Fekete, P. Varga, A. Lehoczki, J.T. Fekete, A. Ungvari, et al., Overweight and obesity significantly increase colorectal cancer risk: a meta-analysis of 66 studies revealing a 25–57% elevation in risk, GeroScience (2024).

[47] L. Nguyen, S. Shanmugan, A review article: the relationship between obesity and colorectal cancer, Curr Diab Rep 25 (1) (2024) 8.

[48] John C. Schell, Kristofor A. Olson, L. Jiang, Amy J. Hawkins, G. Van Vranken Jonathan, J. Xie, et al., A role for the mitochondrial pyruvate carrier as a repressor of the warburg effect and Colon cancer cell growth, Mol Cell 56 (3) (2014) 400–413.

[49] C.L. Bensard, D.R. Wisidagama, K.A. Olson, J.A. Berg, N.M. Krah, J.C. Schell, et al., Regulation of tumor initiation by the mitochondrial pyruvate carrier, Cell Metab. 31 (2) (2020) 284–300. e7.

[50] Y. Ji, C. Yang, Z. Tang, Y. Yang, Y. Tian, H. Yao, et al., Adenylate kinase hCINAP determines self-renewal of colorectal cancer stem cells by facilitating LDHA phosphorylation, Nat. Commun. 8 (1) (2017) 15308.

[51] H.A. Hassan, N.M. Ammar, A. Serag, O.G. Shaker, A.N. El Gendy, A.-H.Z. Abdel-Hamid, Metabolomics driven analysis of obesity-linked colorectal cancer patients via GC-MS and chemometrics: a pilot study, Microchem. J. 155 (2020) 104742.

[52] S. Liu, A. Benito-Martin, F.A. Pelissier Vatter, S.Z. Hanif, C. Liu, P. Bhardwaj, et al., Breast adipose tissue-derived extracellular vesicles from Obese women alter tumor cell metabolism, EMBO Rep. 24 (12) (2023) e57339.

[53] M. Pliszka, L. Szablewski, Glucose transporters as a target for anticancer therapy, Cancers (Basel) 13 (16) (2021).

[54] R. Iftikhar, H.M. Penrose, A.N. King, J.S. Samudre, M.E. Collins, A.B. Hartono, et al., Elevated ATGL in Colon cancer cells and cancer stem cells promotes metabolic and tumorigenic reprogramming reinforced by obesity, Oncogenesis 10 (11) (2021) 82.

[55] S. Dong, S. Liang, Z. Cheng, X. Zhang, L. Luo, L. Li, et al., ROS/PI3K/Akt and Wnt/β-catenin signalings activate HIF-1α-induced metabolic reprogramming to impart 5-fluorouracil resistance in colorectal cancer, J. Exp. Clin. Cancer Res. 41 (1) (2022) 15.

[56] K.T. Pate, C. Stringari, S. Sprowl-Tanio, K. Wang, T. TeSlaa, N.P. Hoverter, et al., Wnt signaling directs a metabolic program of glycolysis and angiogenesis in Colon cancer, EMBO J. 33 (13) (2014) 1454–1473.

[57] B. Chen, C.R. Scurrah, E.T. McKinley, A.J. Simmons, M.A. Ramirez-Solano, X. Zhu, et al., Differential pre-malignant programs and microenvironment chart distinct paths to malignancy in human colorectal polyps, Cell 184 (26) (2021), 6262-80. e26.

[58] P.R. Carr, E. Alwers, S. Bienert, J. Weberpals, M. Kloor, H. Brenner, et al., Lifestyle factors and risk of sporadic colorectal cancer by microsatellite instability status: a systematic review and meta-analyses, Ann. Oncol. 29 (4) (2018) 825–834.

[59] M. Hoffmeister, H. Bläker, M. Kloor, W. Roth, C. Toth, E. Herpel, et al., Body mass index and microsatellite instability in colorectal cancer: a population-based study, Cancer Epidemiol. Biomarkers Prev. 22 (12) (2013) 2303–2311.

[60] D. Lazarova, M. Bordonaro, Hypothesis: mutations and immunosurveillance in obesity-associated colorectal cancer, J. Cancer 13 (10) (2022) 3044–3050.

[61] M. Bordonaro, D. Lazarova, Hypothesis: obesity is associated with a lower mutation threshold in Colon cancer, J. Cancer 6 (9) (2015) 825–831.

[62] M.L. Slattery, K. Curtin, C. Sweeney, T.R. Levin, J. Potter, R.K. Wolff, et al., Diet and lifestyle factor associations with CpG island methylator phenotype and BRAF mutations in colon cancer, Int. J. Cancer 120 (3) (2007) 656–663.

[63] L.A. Hughes, E.J. Williamson, M. van Engeland, M.A. Jenkins, G.G. Giles, J. L. Hopper, et al., Body size and risk for colorectal cancers showing BRAF mutations or microsatellite instability: a pooled analysis, Int. J. Epidemiol. 41 (4) (2012) 1060–1072.

[64] J. Brändstedt, S. Wangefjord, B. Nodin, J. Eberhard, M. Sundström, J. Manjer, et al., Associations of anthropometric factors with KRAS and BRAF mutation status of primary colorectal cancer in men and women: a cohort study, PLoS One 9 (2) (2014) e98964.

[65] J.F. Nabhan, R. Hu, R.S. Oh, S.N. Cohen, Q. Lu, Formation and release of arrestin domain-containing protein 1-mediated microvesicles (ARMMs) at plasma membrane by recruitment of TSG101 protein, Proc. Natl. Acad. Sci. U. S. A. 109 (11) (2012) 4146–4151.

[66] J.A. Welsh, D.C.I. Goberdhan, L. O'Driscoll, E.I. Buzas, C. Blenkiron, B. Bussolati, et al., Minimal information for studies of extracellular vesicles (MISEV2023): from basic to advanced approaches, J. Extracell. Vesicles 13 (2) (2024) e12404.

[67] K. Brennan, K. Martin, S.P. FitzGerald, J. O'Sullivan, Y. Wu, A. Blanco, et al., A comparison of methods for the isolation and separation of extracellular vesicles from protein and lipid particles in human serum, Sci. Rep. 10 (1) (2020) 1039.

[68] G.A. Bray, B.M. Popkin, Dietary fat intake does affect obesity, Am. J. Clin. Nutr. 68 (6) (1998) 1157–1173.

[69] R.M. Pereira, J.D. Botezelli, K.C. da Cruz Rodrigues, R.A. Mekary, D.E. Cintra, J. R. Pauli, et al., Fructose consumption in the development of obesity and the effects of different protocols of physical exercise on the hepatic metabolism, Nutrients 9 (4) (2017).

[70] J.S. Souris, H.J. Zhang, U. Dougherty, N.T. Chen, J.V. Waller, L.W. Lo, et al., A novel mouse model of sporadic colon cancer induced by combination of conditional apc genes and chemical carcinogen in the absence of cre recombinase, Carcinogenesis 40 (11) (2019) 1376–1386.

[71] A. Sivanantham, Y. Jin, Impact of storage conditions on EV integrity/surface markers and cargos, Life 12 (5) (2022).

[72] K.U. Wagner, A. Krempler, Y. Qi, K. Park, M.D. Henry, A.A. Triplett, et al., Tsg101 is essential for cell growth, proliferation, and cell survival of embryonic and adult tissues, Mol. Cell Biol. 23 (1) (2003) 150–162.

[73] A.T. Kong, F.V. Leprevost, D.M. Avtonomov, D. Mellacheruvu, A.I. Nesvizhskii, MSFragger: ultrafast and comprehensive peptide identification in mass spectrometry–based proteomics, Nat. Methods 14 (5) (2017) 513–520.

[74] P.D. Thomas, D. Ebert, A. Muruganujan, T. Mushayahama, L.P. Albou, H. Mi, PANTHER: making genome-scale phylogenetics accessible to all, Protein Sci. 31 (1) (2022) 8–22.

[75] Y. Hu, G.K. Smyth, ELDA: extreme limiting dilution analysis for comparing depleted and enriched populations in stem cell and other assays, J. Immunol. Methods 347 (1) (2009) 70–78.

[76] D.N. Jackson, K.M. Alula, Y. Delgado-Deida, R. Tabti, K. Turner, X. Wang, et al., The synthetic small molecule FL3 combats intestinal tumorigenesis via Axin1-Mediated inhibition of Wnt/β-Catenin signaling, Cancer Res. 80 (17) (2020) 3519–3529.